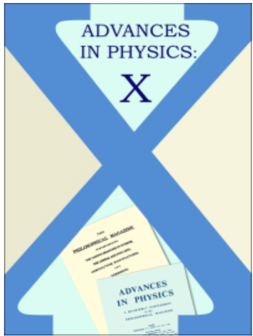


Advances in Physics: X

ISSN: 2374-6149 (Online) Journal homepage: www.tandfonline.com/journals/tapx20

# Spintronics and magnetic memory devices

**Gyung-Min Choi, OukJae Lee, Sunjae Chung, Woojin Kim, Taeyoung Lee, Byong-Guk Park & Seungmo Yang**

**To cite this article:** Gyung-Min Choi, OukJae Lee, Sunjae Chung, Woojin Kim, Taeyoung Lee, Byong-Guk Park & Seungmo Yang (2025) Spintronics and magnetic memory devices, Advances in Physics: X, 10:1, 2557918, DOI: 10.1080/23746149.2025.2557918

**To link to this article:** https://doi.org/10.1080/23746149.2025.2557918

© 2025 The Author(s). Published by Informa UK Limited, trading as Taylor & Francis Group.

Published online: 23 Sep 2025.

Submit your article to this journal

Article views: 3742

View related articles

View Crossmark data

Full Terms & Conditions of access and use can be found at
https://www.tandfonline.com/action/journalInformation?journalCode=tapx20

ADVANCES IN PHYSICS: X
2025, VOL. 10, NO. 01, 1–36
https://doi.org/10.1080/23746149.2025.2557918

REVIEWS

OPEN ACCESS Check for updates

# Spintronics and magnetic memory devices

Gyung-Min Choi[a], OukJae Lee[b], Sunjae Chung[c], Woojin Kim[d], Taeyoung Lee[e], Byong-Guk Park[f] and Seungmo Yang[g]

[a]Department of Energy Science, Sungkyunkwan University, Suwon, Korea; [b]Center for Spintronics, Korea Institute of Science and Technology, Seoul, Korea; [c]Department of Physics Education, Korea National University of Education, Cheongju, Korea; [d]Compute & Memory Department, IMEC, Leuven, Belgium; [e]Foundry Business, Samsung Electronics Co., Giheung, Korea; [f]Department of Materials Science and Engineering, KAIST, Daejeon, Korea; [g]Quantum Technology Institute, Korea Research Institute of Standards and Science, Daejeon, Korea

**ABSTRACT**
Spintronics technology enables electrical reading and writing of magnetization orders, thus have led to development of magnetic random access memory (MRAM). Owing to its superior properties of size, speed, and endurance, MRAM is promising for applications in internet-of-things, automotive microcontrollers, and data centers. Here, we review key spintronic technologies of magnetoresistance and spin-transfer torque, which are the operating mechanism for MRAM, and properties and status of MRAM commercialization. We also review recent achievements and future challenges in emerging topics of spin-orbit torque, voltage gating, orbitronics, and antiferromagnetic spintronics, and new applications of spin-torque oscillators, probabilistic computing, and skyrmion-based applications.

**ARTICLE HISTORY**
Received 25 June 2025
Accepted 2 September 2025

**KEYWORDS**
Spintronics; magnetic memory; MRAM

**GRAPHICAL ABSTRACT**

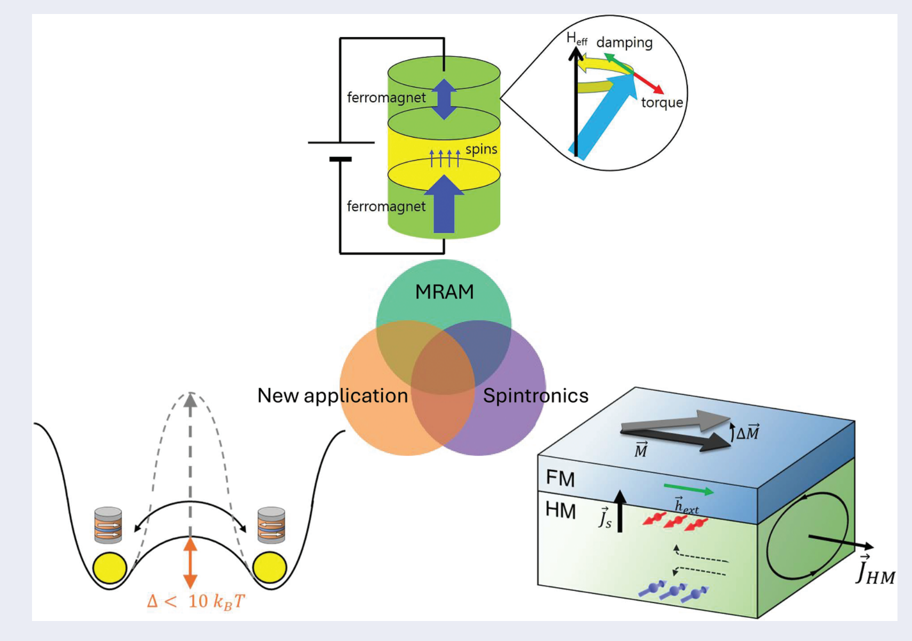


## 1. Introduction

Ferromagnetic magnetization provides a robust foundation for information technology and has been crucial to the development of modern storage devices such as hard disk drive and magnetic tape storage. Hard disk drives

**CONTACT** Gyung-Min Choi gmchoi@skku.edu Department of Energy Science, Room 86582, N center, Sungkyunkwan University, 2066 Seobu-ro, Jangan-gu, Suwon 16419, Korea

© 2025 The Author(s). Published by Informa UK Limited, trading as Taylor & Francis Group. This is an Open Access article distributed under the terms of the Creative Commons Attribution-NonCommercial License (http://creativecommons.org/licenses/by-nc/4.0/), which permits unrestricted non-commercial use, distribution, and reproduction in any medium, provided the original work is properly cited. The terms on which this article has been published allow the posting of the Accepted Manuscript in a repository by the author(s) or with their consent.

are widely used in computers and data centers for their massive data capacity [1], and magnetic tape storage is favored for archives and backups due to its affordability and long retention time [2]. A key limitation of both technologies, however, is their dependence on mechanical reading and writing mechanisms. The mechanical access to individual memory cells, tied to the rotational speed of the disk and the movement of the read/write head, results in slow access times and significant power consumption [1,2]. To enable fast and low-power access, electrical reading and writing mechanisms are required.

Spintronics aims for electrical manipulation of spin of electrons and magnetization of ferromagnets [3–6]. This capability underpins both electrical reading and writing mechanisms. Electrical reading is achieved through magnetoresistance, a phenomenon stemming from the interaction between magnetization and charge current. Electrical writing is facilitated by spin-transfer torque, which describes the interaction between the spins of itinerant electrons and the magnetization of localized electrons. Magnetic random access memory (MRAM) leverages magnetoresistance for reading and spin-transfer torque for writing, enabling electrical access to memory cells. Now commercialized by several semiconductor companies as standalone or embedded application [7,8], MRAM is a highly promising non-volatile memory solution due to its durability, speed, and energy efficiency.

Spintronics has diversified into several active research areas, including spin-orbit torque (SOT), voltage-controlled magnetic anisotropy (VCMA), orbitronics, and antiferromagnetic spintronics. SOT, which utilizes charge-to-spin conversion in nonmagnetic materials to exert spin torque on ferromagnets, shows promise for fast cache memory applications. VCMA leverages the electric-field effect on magnetic anisotropy energy, offering a path toward ultralow power consumption. Orbitronics, an emerging field, seeks to control the orbital degree of freedom of electrons, with recent studies demonstrating successful electrical manipulation of non-equilibrium orbital states. Antiferromagnets offer advantages over ferromagnets, such as high resonance frequency and stability against field perturbation. Despite their lack of net magnetization, recent breakthroughs have enabled efficient electrical reading and writing of antiferromagnetic orders.

Beyond memory, advancements in spintronics are enabling new device structures. When spin torque precisely balances magnetic damping, continuous magnetization precession becomes possible. The high-frequency signals generated by such spin-torque oscillators hold potential for wireless communication, sensors, and neuromorphic computing. Furthermore, by reducing thermal stability, the deterministic nature of magnetization switching can be altered to become stochastic. This stochastic behavior can be harnessed for probabilistic computing, offering a powerful approach for solving complex optimization problems that are intractable for classical von Neumann architectures. In addition, magnetic skyrmions, topological spin textures, offer unique advantages for spintronic applications. Their nanoscale size, topological stability, and particle-like dynamics make them ideal candidates for various device concepts. Recent demonstrations of skyrmion-based synapses, transistors, racetrack memories, and reservoir computing units highlight their potential for low-power, high-density computing with unprecedented functionalities.

In this review, we summarize recent progress in spintronics and its applications. Section 2 explains research advancements in MRAM's electrical reading and writing mechanisms: magnetoresistance and spin-transfer torque. We also discuss MRAM's status and its development for various applications. Section 3 delves into new spintronic research topics, including spin-orbit torque, voltage gating, orbitronics, and antiferromagnetic spintronics. Section 4 covers new applications of spintronics, specifically spin-torque oscillators, probabilistic computing, and skyrmion-based applications. Finally, we offer an outlook on remaining challenges and future research directions.

## 2. Development of MRAM

### 2.1. Magnetoresistance

The electrical detection of magnetization direction relies on magnetoresistance, a coupling of electrical resistance and magnetization. This effect is broadly classified into three types (Figure 1): anisotropic magnetoresistance (AMR), giant magnetoresistance (GMR), and tunneling magnetoresistance (TMR). AMR arises from the scattering between *s*-electrons (conduction electrons) and *d*-electrons (localized electrons) within a single ferromagnetic material, with typical values of than 1% at room temperature [9–12]. GMR, discovered in 1988, is observed in structures composed of alternating ferromagnetic and nonmagnetic conductive layers

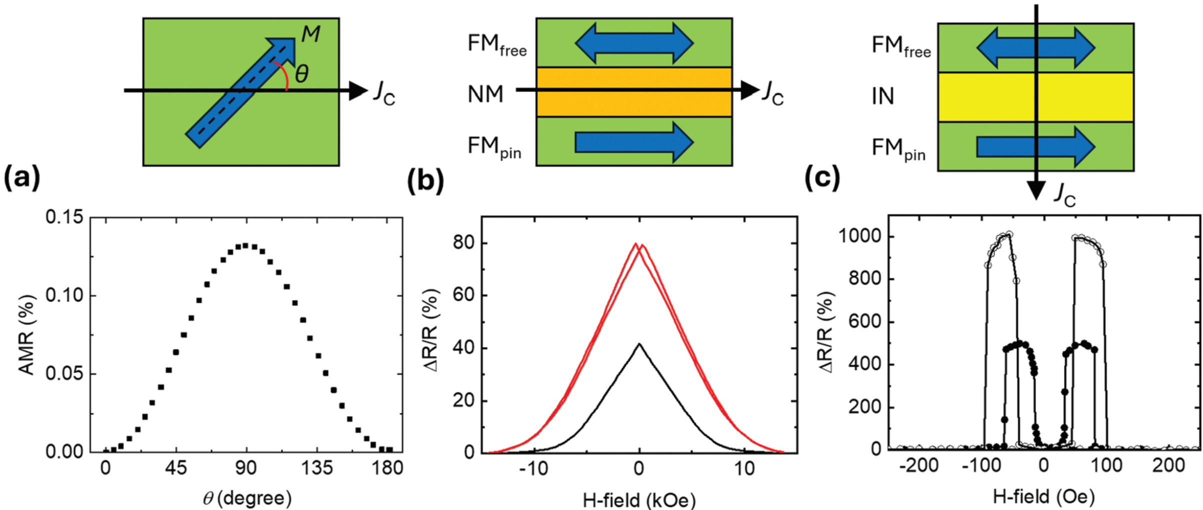


**Figure 1.** Magnetoresistance. (a) Anisotropic magnetoresistance of a Fe film at room temperature. The figure is reproduced with permission from ref [10]. (b) Giant magnetoresistance of $[Co/Cu]_{xn}$ multilayers at 4.2 K (red line) and 295 K (black line). The figure is reproduced with permission from ref [15]. (c) Tunneling magnetoresistance of CoFeB/MgO/CoFeB junction at 5 K (open circle) and 300 K (filed circle). The figure is reproduced with permission from ref [33].

[13,14]. The GMR value is quantitatively expressed as $\Delta R/R = (R_{AP} - R_P)/R_P$, where $R_{AP}$ and $R_P$ represent the resistance for antiparallel and parallel magnetization alignments, respectively. Reported GMR values can be as high as a few tens of percent at room temperature in repetitive multilayer stacks [15–17].

TMR was first observed in 1975 in an Fe/Ge-O/Co junction with a value of 14% at 4.2 K [18]. This phenomenon occurs in a magnetic tunnel junction (MTJ), where charge current flows *via* electron tunneling through an insulating (IN) spacer within an FM/IN/FM structure. Later, TMR has extended to room temperature using an aluminum oxide ($AlO_x$) barrier [19,20]. Optimizing the growth conditions of the $AlO_x$ barrier and ferromagnetic electrodes, TMR values have increased to over 70% [21,22]. According to the Julliere formula of $2P_1P_2/(1{-}P_1P_2)$, where $P_1$ and $P_2$ are the spin polarizations of the two magnetic layers, a TMR of 70% is close to the theoretical maximum, considering reported tunneling spin polarization values of approximately 0.5 for CoFe electrodes [23,24]. Theory predicted even larger TMR value over 1000% in epitaxial Fe(001)/MgO(001)/Fe(001) structures [25,26], which was attributed to the spin-dependent tunneling through the epitaxial MgO(001) barrier [25,26]. Experimental confirmation was achieved in 2004: 180% TMR with epitaxial Fe/MgO/Fe junctions and 220% TMR with textured CoFe/MgO/CoFe junctions [27,28]. Subsequent advancements in epitaxial MTJ growth using molecular beam epitaxy, sputter deposition, and electron-beam evaporation on single-crystalline MgO substrates have pushed room-temperature TMR values to 410% with body-centered cubic (bcc) Co, 417% with bcc Fe, and 631% with bcc CoFe electrodes [29–31]. For mass production of MTJs, which need to be grown on thermally oxidized Si substrates, a key challenge was the structural incompatibility between the (111) texture of the face-centered cubic (fcc) pinning layer and the (001) texture of the NaCl MgO barrier. The use of an amorphous CoFeB electrode provided the solution [32]; (001) textured MgO could grow on the amorphous CoFeB, which subsequently served as a template for bcc crystallization of CoFeB during a post-annealing step. Optimization for (001) textured MTJs, involving careful control of CoFeB and MgO growth and composition, has resulted in high TMR values of 604% at room temperature and 1144% at 5 K [33,34], nearly achieving the same peak values as epitaxial MTJs.

TMR has extended to a variety of barrier and electrode materials. $MgAl_2O_4$ was employed to reduce lattice mismatch with bcc Fe, leading to reported TMR values of 429% in epitaxial MTJs and 240% in textured MTJs [35,36]. To decrease the resistance of MTJs by modifying the barrier's bandgap, materials like $MgGa_2O_4$ and MgXO (where X represents doping elements such as Ti, Fe, or Mn) were explored, with TMR values exceeding 100% [37–39]. Another approach focused on enhancing electrode spin polarization using Heusler-type half-metals, including CoFeAl, CoFeAlSi, $Co_2$(Mn,Fe)Si, and CoMnFe, which achieved high room-temperature TMR values over 300% [40–43]. However, the complex crystal structures of Heusler compounds have largely

limited their application to epitaxial MTJs. To improve thermal stability, researchers utilized electrodes exhibiting perpendicular magnetic anisotropy, such as $L1_0$ FePt and tetragonal MnGa, which delivered TMR values exceeding 100% [44,45]. Textured growth of $L1_0$ FePt on Si substrate using an MgO template is possible [46]; however, its relatively modest TMR and the high annealing temperatures are challenging issues. Alternatively, interfacial anisotropy between CoFeB and MgO has emerged as a promising strategy to achieve both enhanced thermal stability and high TMR [47–49]. TMR reports utilizing various electrode and barrier materials were summarized in Table 1.

### 2.2. Spin-transfer torque

To electrically switch magnetization, spin-transfer torque (STT) is employed, which harnesses the interaction between localized magnetization and a spin current (Figure 2). STT operates through two distinct processes: the generation of a spin current from a pinned layer and its subsequent absorption by a free layer. Spin generation in metallic spin valves relies on spin-dependent conductivities [50–52], while in magnetic tunnel junctions (MTJs), it leverages spin-dependent tunneling [23,24]. When the spin current is injected to a free layer, the transverse component of the conduction electrons' spin polarization is absorbed by the free layer's magnetization [53–57]. As a direct consequence of angular momentum conservation, STT applies a torque on the magnetization. Depending on the torque vector, STT further distinguished to the damping-like torque along the $\mathbf{m} \times (\mathbf{m} \times \sigma)$ and field-like torque along the $\mathbf{m} \times \sigma$, where $\mathbf{m}$ is the unit vector of the magnetization of the free layer and $\boldsymbol{\sigma}$ is the unit vector of the spin polarization of the conduction electrons. Because of strong dephasing, STT is often dominated by damping-like torque [47], whose magnitude is described as $\tau_{\mathrm{DL}} = \frac{J_s}{M_S d_{\mathrm{FM}}}$, where $J_s$ is the input spin current density, $M_S$ is the saturation magnetization of the free layer, and $d_{\mathrm{FM}}$ is the thickness of the free layer. However, in cases of incomplete dephasing, field-like torque can be significant [58–60]. Note that STT vanishes at exact collinear (parallel or antiparallel) alignment of $\mathbf{m}$ and $\boldsymbol{\sigma}$. Therefore, to initiate STT, an initial non-collinear alignment or a long incubation delay time, in which thermal agitation deviates the collinear alignment, is required [61–63].

The initial discovery of STT-driven magnetization dynamics occurred in spin valve systems, which consist of two ferromagnetic layers separated by a conductive spacer such as copper. In this structure, a charge current passing through the spin valve causes spin polarization from the thick, 'pinned' ferromagnetic layer to exert a torque on the thin, 'free' ferromagnetic layer. Within nano-pillar structures designed for precise current paths, a current density below $10^8$ A cm$^{-2}$ achieves complete magnetization switching [64–66]. STT can also induce a coherent precession of the magnetization [67–70]. Following the discovery of large TMR, STT-induced dynamics were investigated in MTJs, leading to reports of both STT-driven magnetization switching and coherent precession. Significantly, MTJs achieved a low switching current density of approximately $10^6$ A cm$^2$ [49,71]. This low current is crucial for integration with Si transistors, reducing operational power and extending the tunneling barrier's lifetime. Even lower switching currents, while maintaining high thermal stability, have been realized with modified MTJ structures such as dual barriers and synthetic free layers [72–74]. However, when current pulses are shorter than 10 ns, thermal activation becomes inefficient, causing

**Table 1.** Summary of TMR reports of MTJs with various electrodes and barriers at room temperature (300 K) and low temperature (<10 K).

| structure | electrode | barrier | TMR (300 K) | TMR ( < 10 K) | Reference |
|---|---|---|---|---|---|
| epitaxial | Co | MgO | 410 | 507 | [29] |
| epitaxial | Fe | MgO | 417 | | [30] |
| epitaxial | CoFe | MgO | 631 | 1143 | [31] |
| textured | CoFeB | MgO | 604 | 1144 | [34] |
| epitaxial | Fe | $MgAlO_x$ | 429 | 1034 | [35] |
| textured | CoFeB | $MgAlO_x$ | 240 | | [36] |
| epitaxial | Fe | $MgGa_2O_4$ | 121 | 196 | [37] |
| textured | CoFeB | Doped MgO | > 150% | | [38,39] |
| epitaxial | $Co_2FeAl$ | $MgAl_2O_4$ | 342 | 616 | [40] |
| epitaxial | $Co_2FeAl_{0.5}Si_{0.5}$ | MgO | 386 | 832 | [41] |
| epitaxial | $Co_2(Mn,Fe)Si$ | MgO | 429 | 2610 | [42] |
| epitaxial | CoMnFe | MgO | 350 | 1002 | [43] |
| textured | FePt | MgO | 100 | | [44] |
| epitaxial | MnGa | MgO | 118 | 260 | [45] |

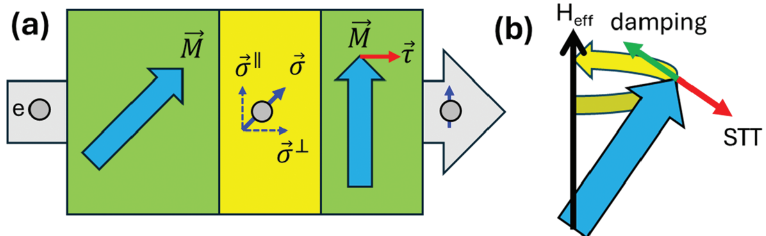


**Figure 2.** Schematics of spin-transfer torque (STT). (a) Electrons that flow through a pinned layer became spin polarized ($\sigma$) along the magnetization (M). Spin polarization consists of parallel ($\sigma^{\parallel}$) and orthogonal ($\sigma^{\perp}$) components with respect to the magnetization of the free layer. The orthogonal component is quickly absorbed by the free layer and induces a torque ($\tau$). (b) STT-driven dynamics of magnetization. When STT becomes larger than magnetic damping, magnetization precesses along the effective field ($H_{eff}$) and eventually leads to switching.

a rapid increase in switching current [75]. Thus, thermal activation process limits the writing speed of memory devices. In the fully thermal-activated region with long current pulses, the switching current density ($J_c$) is determined by (in SI units):

$$J_c = \frac{2e}{\hbar}\alpha\frac{M_S H_K d_{FM}}{2P_s}, \tag{1}$$

where $e$ is the elementary charge, $\hbar$ is the reduced Plank constant, $\alpha$ is the damping constant, $H_K$ is the anisotropy field, and $P_s$ is the spin polarization from the pinned layer. With a reading mechanism of TMR and writing mechanism of STT, STT-MRAM has been commercialized. Furthermore, STT in MTJ induces a coherent precession, generating significant RF power due to hight TMR [76].

### *2.3. Status of MRAM*

An MRAM device integrates a CMOS transistor with a magnetic tunnel junction (MTJ). After silicon transistor fabrication, the MTJ stack is deposited via sputtering, typically consisting of an underlayer, pinned layer, MgO barrier, free layer, and capping layer (Figure 3(a)) [71–74]. Often, a synthetic antiferromagnet structure, utilizing exchange bias with an antiferromagnet [77], forms the pinned layer to ensure fixed magnetization and minimize stray fields. CoFeB alloy is chosen for both pinned and free layers due to its crystalline structure, which enables high TMR, and its interface, which supports perpendicular magnetic anisotropy [49]. Following film deposition, a post-annealing process is crucial to induce the (001) texture in CoFeB and set the exchange bias pinning. Key properties of the unpatterned MTJ films are then characterized. TMR is evaluated using a current-in-plane tunneling technique [78], while magnetic properties like saturation magnetization, coercivity, exchange bias, anisotropy energy, and damping constant are assessed using a magneto-optical Kerr microscope, vibrating sample magnetometer, and ferromagnetic resonance [79–81]. The patterning of MTJ films into nanoscale cells is performed via ion beam etching or plasma-based etching (Figure 3(b)) [82,83]. For long-term reliability, it is crucial to remove metallic sidewalls (which can cause short failures) and suppress defects like pinholes and edge damage during etching [84]. After patterning, the switching behavior of individual MTJ cells and the statistical distribution across MTJ arrays are evaluated. Figure 3(c) illustrates patterned MTJ cells integrated onto silicon transistors. Figure. 3(d–f) represents typical test results during the MRAM fabrication.

For the reliability of MRAM, key indicators include the distribution of resistance, write energy, error rate of write, endurance, and data retention. In reading operations, a high TMR and clear separation between parallel and antiparallel resistances are crucial (Figure 4(a)). A read margin, quantified as a ratio of TMR to resistance distribution width, ideally needs to be greater than 20 [85]. The writing operation is governed by both the operating bias (determining current density) and pulse duration (influencing thermal activation) [75]. To ensure reliable writing, the operating parameters are selected to achieve a write-error rate in the parts-per-million (ppm) range. Write energy per bit is calculated by combining MTJ resistance, cell area, writing current density, and current duration. Recently, a record-low write energy of 10 pJ per bit was reported

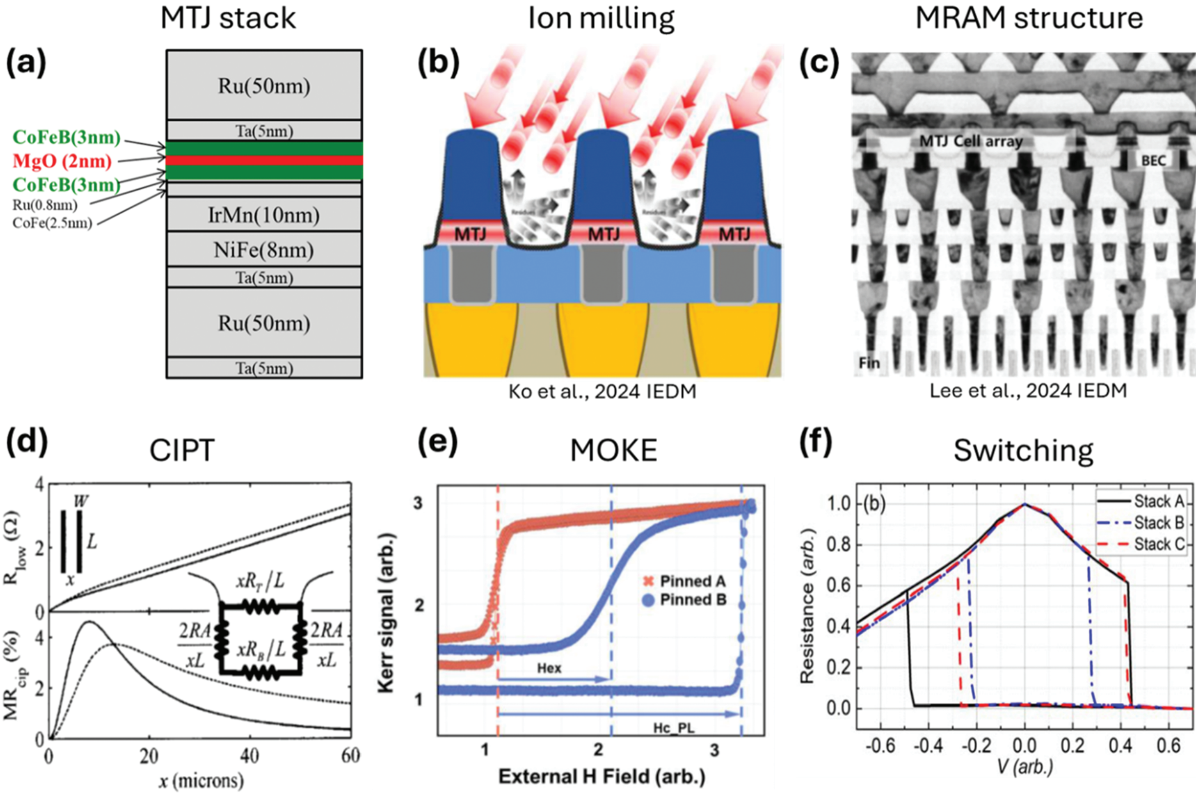


**Figure 3.** MRAM fabrication and test procedures. (a) a typical film layout of a magnetic tunnel junction (MTJ). (b) Nano pattering using an ion milling. The figure is reproduced with permission from ref [87]. (c) a cross-sectional picture of a fabricated MRAM structure. The figure is reproduced with permission from ref [86]. (d) Current-in-plane-tunneling (CIPT) tests tunneling magnetoresistance of MTJ films before pattering. The figure is reproduced with permission from ref [78]. (e) Magneto-optical Kerr effect (MOKE) tests coercivity ($H_c$) and exchange-bias ($H_{ex}$) fields of MTJ films. The figure is reproduced with permission from ref [87]. (f) Electrical probe station tests switching behavior of individual MTJ cells after patterning. The figure is reproduced with permission from ref [91].

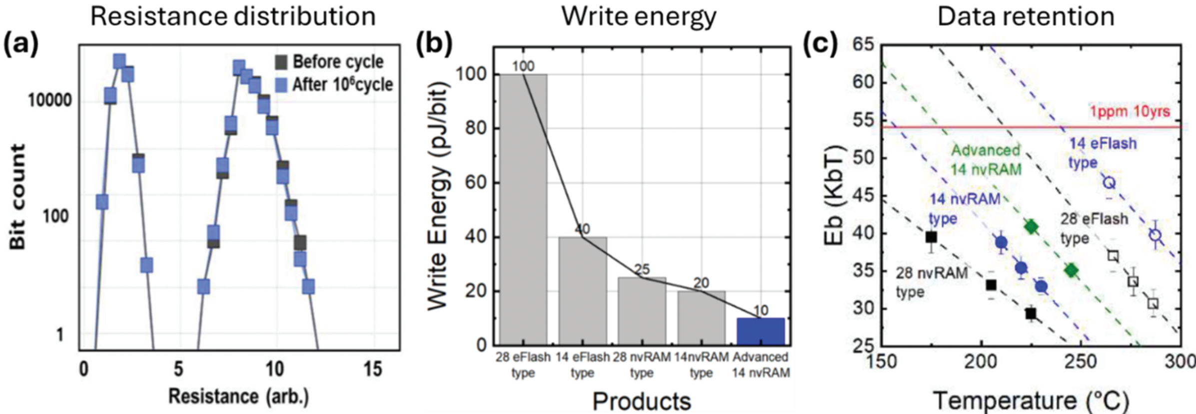


**Figure 4.** Key properties of MRAM. (a) Magnetoresistance distributions of MRAM cells before and after $10^6$ operation cycles. The figure is reproduced with permission from ref [87]. (b) Write energy per bit operation with different node technology. The figure is reproduced with permission from ref [86]. (c) Temperature-dependent energy barriers of MRAM cells for data retention over 10 years. The figure is reproduced with permission from ref [86].

using an advanced 14 nm embedded-MRAM process [86] (Figure 4(b)). In terms of endurance, wafer-level cycling tests for reading and writing demonstrated a high endurance of $10^{12}$ cycles [86,87]. Data retention, the duration for which data can be reliably stored, is another critical reliability attribute. It is determined by the free layer's energy barrier ($E_b$), which can be evaluated from the temperature-dependent or pulse-width-dependent

**Table 2.** Specification of commercialized MRAM products for applications of IoT connectivity and automotive microcontroller unit (MCU).

| Application type | | Logic node (nm) | Cell size ($\mu m^2$) | Temp. range (°C) | Write speed (ns) | Read speed (ns) | Retention | En-durance | Ref. |
|---|---|---|---|---|---|---|---|---|---|
| IoT | Flash type | 22 ~ 28 | 0.036 ~ 0.046 | −40 ~ 125 | 200 | 10 ~ 15 | 10 years at ~ 150°C | > $10^5$ | [88–90] |
| | NVRAM type | | | −40 ~ 85 | 100 | 10 ~ 15 | 10 years at < 90°C | $10^{12}$ | |
| IoT/Auto MCU | Flash type | 14 ~ 16 | 0.024 ~ 0.033 | −40 ~ 150 | 100 ~ 200 | 10 | 20 years at 150°C | > $10^6$ | [86,91] |
| | NVRAM type | | | −40 ~ 125 | 50 ~ 100 | 10 | 10 years at 85 ~ 150°C | $10^{14}$ | |
| Auto MCU | Flash type | 5 ~ 8 | 0.011 ~ 0.017 | −40 ~ 150 | 100 ~ 200 | < 10 | 20 years at 150°C | > $10^6$ | [87] |
| | NVRAM type | | | −40 ~ 125 | 20 ~ 50 | < 10 | 10 years at < 90°C | $10^{14}$ | |

switching current density ($J_c$) using the following relation [75]:

$$J_c = J_{c0}\left(1 - \frac{k_B T}{E_b}\ln\frac{t_p}{\tau_0}\right), \tag{2}$$

where $k_B$ is the Boltzmann constant, $T$ is the temperature, $E_b$ is the energy barrier of the free layer, $t_p$ is the current pulse width, $\tau_0$ is the inverse of the attempt frequency, and $J_{c0}$ is the critical current density at $t_p = \tau_0$. To improve $E_b$ of the free layer, interface engineering for perpendicular anisotropy or synthetic antiferromagnetic structure for exchange biasing was employed [49,72–74]. By optimizing the free layer structure and fabrication process, a long data retention of >10 year at 150°C has been achieved [86] (Figure 4(c)).

Embedded non-volatile memory (eNVM) is crucial for code and data storage in microcontroller units (MCUs), a role traditionally dominated by embedded Flash. However, Flash's scalability beyond the 28 nm node is limited. Consequently, major foundries have developed alternative eNVMs like MRAM, resistive random access memory (RRAM), and phase-change random access memory (PCRAM). Among these, embedded MRAM has achieved mass production, initially targeting wearable and Internet-of-Things (IoT) applications [88–90]. More recently, embedded MRAM has demonstrated its efficacy in automotive MCU and data center applications [86,87,91]. STT-MRAM is well suited for automotive-grade applications, which demand continuous data logging and updates, due to its small cell size, reliable operation at high temperatures (up to 150°C), fast write/read speeds, superior data retention, and high endurance. Especially, STT-MRAM is an ideal eNVM solution at FinFET nodes below 22 nm, significantly improving performance and reliability in modern automotive systems. For data center applications, high-bandwidth, low-power consumption, and near-unlimited endurance (up to $10^{14}$ cycles) are important for data transfers between computing units and external memory. Table 2 summarizes specifications of commercialized STT-MRAM products with different application types.

With the advent of artificial intelligence, new computer architecture of neuromorphic computing is sought to reduce power consumption. Recently, process-in-memory, a prominent example of neuromorphic computing, was demonstrated using crossbar arrays of MTJs [92]. Other than MTJ, array of spin-torque oscillator is also a promising system for neuromorphic computing for its nonlinear and tunable dynamics (Section 4.1). The superparamagnetic MTJ has been implemented for probabilistic computing for its tunable stochastic nature (Section 4.2). Both MTJ and spin-torque oscillator are based on dynamics of spatially uniform magnetization. Spatially varying magnetic texture can be employed for spintronic applications. Especially, skyrmion, topological spin texture, is promising for a memory application of racetrack memory and for new computing application (Section 4.3).

## 3. New research topics of spintronics

### *3.1. Spin-orbit torque*

While STT relies on spin current generated from ferromagnetic materials, spin Hall effect (SHE) and Rashba-Edelstein effect (REE) offer alternative methods for spin generation from non-ferromagnetic materials [93,94]. SHE is a bulk phenomenon where an applied charge current ($J_c$) induces a transverse spin current ($J_s$), defined as $J_s = \theta_{SH} J_c$, where $\theta_{SH}$ is the spin Hall angle, representing the charge-to-spin conversion efficiency. The induced spin polarization is orthogonal to both $J_c$ and $J_s$ directions [93]. In contrast, REE converts $J_c$ into spin accumulation at interface with broken inversion symmetry [94]. The spin accumulation driven by REE is proportional to Rashba spin splitting, and its spin polarization is orthogonal to the charge current and the direction of inversion-symmetry breaking. Despite their distinct mechanisms, experimentally differentiating

SHE and REE can be challenging, especially at heterostructure interfaces where the resulting spin polarization direction is identical for both effects (Figure 5) [95].

While SHE and REE were initially studied in semiconductors [96–98], a significant breakthrough for their practical application occurred in metallic systems: SHE- or REE-driven magnetization switching was achieved using heterostructures of heavy metals and ferromagnets [99–102]. This torque, distinct from STT, is termed spin-orbit torque (SOT). When SOT is employed for switching perpendicular magnetic anisotropy, the switching current density is estimated as (assuming the anisotropy field $H_K$ is much larger than the applied field) [103]:

$$J_c = \frac{2e}{\hbar}\frac{M_S H_K d_{FM}}{2\theta_{SH}}. \quad (3)$$

For practical application of SOT, the charge-to-spin conversion efficiency of $\theta_{SH}$ is the critical factor. An advantage of SOT over STT is its orthogonality between spin polarization and magnetization, which eliminates the need for an incubation delay for thermal agitation. Furthermore, because the writing charge current flows through the heavy metal rather than the MgO barrier, SOT-MRAM has superior reliability compared to STT-MRAM [102].

To accurately quantify $\theta_{SH}$, three experimental techniques of spin-torque ferromagnetic resonance (ST-FMR), harmonic Hall voltage (HHV), and magneto-optical Kerr effect (MOKE) were widely used (Figure 6). ST-FMR detects SOT-driven magnetization precession with the assistance of AMR. When a microwave (RF) charge current is applied in-plane to a HM/FM bilayer, the spin current ($J_s$) from HM along with the Oersted field ($H_{Oe}$) induces magnetization oscillation of FM [100,104]. The resulting resistance oscillation from AMR mixes with the RF charge current, generating a DC mixing voltage [100]. A ratio between the symmetric and antisymmetric parts of the mixing voltage provides a determination of $\theta_{SH}$=$J_s/J_c$. HHV measures the steady-state equilibrium of magnetization in the presence of SOT [105]. When the oscillation frequency of charge current is much smaller than the FMR frequency, SOT acts as an effective field: $\tau_{DL}$-driven field of $\mathbf{H}_{DL} \sim \mathbf{m} \times \sigma$ and $\tau_{FL}$-driven field of $\mathbf{H}_{FL} \sim \sigma$, where $\mathbf{m}$ and $\boldsymbol{\sigma}$ are the unit vector for magnetization and spin polarization, respectively [106]. The resultant tilting of to a new equilibrium can be detected *via* Hall resistance of FM. Distinction between $H_{DL}$ and $H_{FL}$+$H_{Oe}$ is possible from the angle dependence between the charge current and magnetization. Often, charge current induces an out-of-plane temperature gradient, which causes a transverse thermoelectric signal, such as anomalous Nernst effect (ANE) [106]. Therefore, the external field ($H_{ext}$) dependence is required to distinguish SOT from ANE. MOKE optically detects the SOT-driven magnetization tilting [107,108]. MOKE detects the SOT-driven tilting of magnetization *via* magneto-optic constant of FM. The polarization angle of light is varied to distinguish $H_{DL}$ and $H_{FL}$+$H_{Oe}$. MOKE has an additional signal of the out-of-plane Oersted field ($H_{Oe}^z$) owing to its spatial resolution, and $H_{Oe}^z$ can be used to determine the magneto-optic constant. Distinction between $H_{DL}$ and $H_{Oe}^z$ can be achieved by analyzing the spatial position dependence and the polarity dependence on $H_{ext}$.

SOT has been extensively studied in 5d heavy metals (HMs). Platinum (Pt) exhibits a positive $\theta_{SH}$ of approximately 0.1, while tantalum (Ta), tungsten (W), and hafnium (Hf) show negative $\theta_{SH}$ values ranging from −0.1 to −0.3 [100,102,109–112]. The intrinsic SHE magnitude is attributed to orbital Hall effect and spin-orbit coupling, with the sign of $\theta_{SH}$ explained by electron filling in the 5d band [113,114]. To further

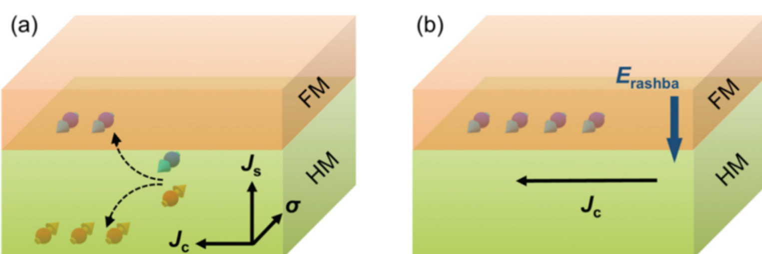


**Figure 5.** Schematics of spin Hall effect (SHE) and Rashba-Edelstein effect (REE). (a) SHE converts a charge current ($J_c$) to a transverse spin current ($J_s$) inside HM. $J_s$ is incident on a ferromagnet (FM) to induce a torque. (b) REE converts a charge current to spin polarization (arrows) at the HM/FM interfaces. The figure is reproduced with permission from ref [95].

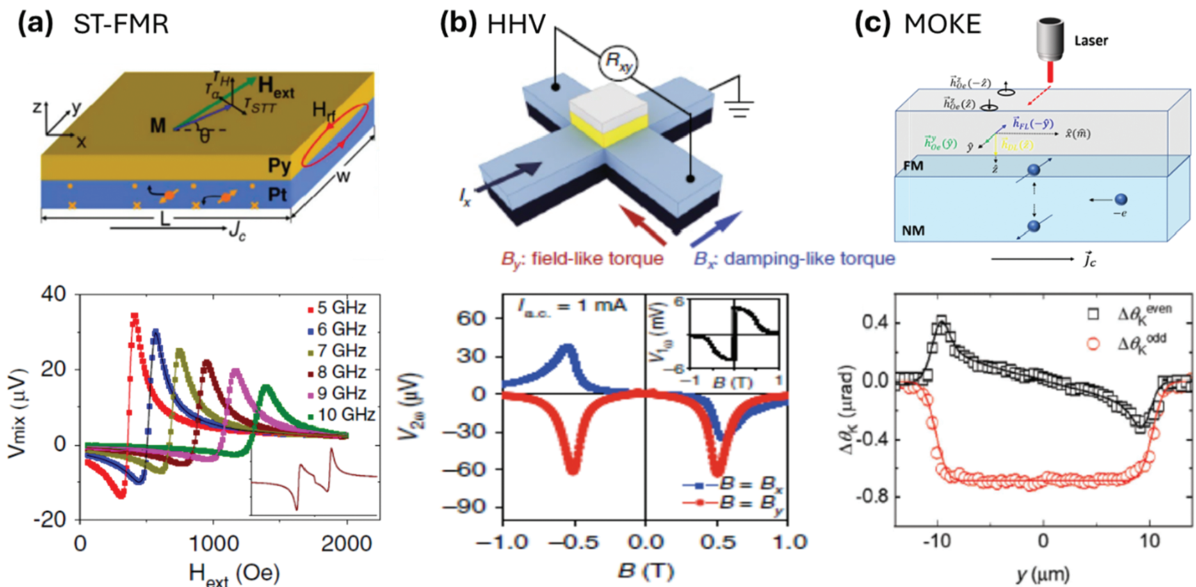


**Figure 6.** SOT measurement technique. (a) Spin-torque ferromagnetic resonance (ST-FMR) measurement of SOT in the Ta/CoFeB structure. The figure is reproduced with permission from ref [100]. (b) Harmonic Hall voltage (HHV) measurement of SOT in the Ta/CoFeB structure. The figure is reproduced with permission from ref [137]. (c) Magneto-optical Kerr effect (MOKE) measurement of SOT in the Bi/CoFeB structure. The figure is reproduced with permission from ref [125].

**Table 3.** Summary of spin Hall angle ($\theta_{SH}$) and electrical resistivity ($\rho_{NM}$) of various nonmagnetic systems, including heavy metal (HM), alloy, topological insulator (TI), and semimetal (SM).

| Class | Structure | Method | $\lvert\theta_{SH}\rvert$ | $\rho_{NM}$ (μΩ cm) | Ref. |
|---|---|---|---|---|---|
| HM | Pt(6)/Py(4) | ST-FMR | 0.08 | 20 | [100] |
| | Pt(3)/Co(0.6) | HHV | 0.16 | 36 | [109] |
| | Ta(8)/CoFeB(4) | ST-FMR | 0.15 | 190 | [102] |
| | Ta(1.5)/CoFeB(1) | HHV | 0.03 | 191 | [110] |
| | W(6)/CoFeB(5) | ST-FMR | 0.3 | 170 | [111] |
| | Hf(1 ~ 20)/CoFeB(1) | HHV | 0.33 | 154 | [112] |
| Alloy | $Pt_{0.75}Au_{0.25}$ | HHV | 0.35 | 83 | [115] |
| | $Pt_{0.69}Cr_{0.31}$ | HHV | 0.9 | 133 | [116] |
| | $W_{0.8}V_{0.2}$ | HHV | 0.5 | 180 | [117] |
| | $HM_xAl_{1-x}$ | ST-FMR | ~1 | ~1000 | [118] |
| | $IrMn_3$ | ST-FMR | 0.2 | 160 | [119] |
| | PtMn | ST-FRM | 0.19 | 150 | [120] |
| TI | $Bi_2Se_3$(8)/Py(8) | ST-FMR | 3.5 | 1800 | [121] |
| | $Bi_2Se_3$(5)/CoFeB(7) | ST-FMR | 1.75 | 4100 | [122] |
| | $Bi_xSe_{1-x}$(4)/CoFeB(5) | HHV | 18.6 | 12800 | [123] |
| | $(BiSb)_2Te_3$/CoFeB(1.4) | HHV | 2.5 | 5500 | [124] |
| | SnTe/Ti(2)/CoFeB(1.4) | HHV | 1.4 | 1800 | [124] |
| SM | $WTe_2$(122)/Py(6) | ST-FMR | 0.51 | 580 | [132] |
| | $MoTe_2$(83)/Py(6) | ST-FMR | 0.27 | 542 | [133] |
| | Bi(20)/CoFeB(5) | MOKE | 0.5 | 1400 | [125] |

enhance $\theta_{SH}$, alloying strategies have been employed, yielding high $\theta_{SH}$ values of >0.3 in $Pt_{1-x}Au_x$, $Pt_{1-x}Cr_x$, $W_{1-x}V_x$, $HM_{1-x}Al_x$, and $Ir_{1-x}Mn_x$ alloys [115–120]. The enhanced SOT efficiency in these alloys is often attributed to extrinsic SHE due to impurities. Much higher $\theta_{SH}$ values were reported with topological insulators and semimetals, such as Bi, $Bi_2Se_3$, $(BiSb)_2Te_3$, and SnTe [121–125]. With surface spin-momentum locking of topological insulators, $\theta_{SH}$ values can exceed one. However, high resistivity and the absence of large-scale growth techniques pose significant challenges for the application of topological insulators. Table 3 summarizes SOT efficiency reported for various nonmagnetic materials.

Note that conventional SOT with in-plane spin polarization cannot deterministically switch perpendicular magnetization and requires an external in-plane magnetic field along the current direction. To eliminate the need for such an external field, several strategies have been proposed. Engineered symmetry breaking, such as lateral structural asymmetry and tilted anisotropy, has been employed for field-free switching [126–128].

Materials with low crystalline symmetry, such as $L1_0$-ordered CuPt, tetragonal $MnPd_3$, and two-dimensional semimetals, can also enable field-free switching [129–133]. The antiferromagnetic phase of PtMn or IrMn allows field-free switching by generating an effective in-plane magnetic field [134,135]. Utilizing hybrid spin sources, such as SOT-STT combination or magnetic trilayer, can also allow field-free switching [136,137].

Given its efficient spin generation in nonmagnetic materials, SOT is now a leading candidate for the writing mechanism in MRAM (SOT-MRAM). Its sub-nanosecond switching speed and virtually unlimited endurance are particularly attractive for cache memory applications [138]. For SOT-MRAM realization, SOT materials and structures must be compatible with existing MRAM fabrication processes. Heavy metals like Ta and W have demonstrated compatibility with the perpendicular magnetic anisotropy of CoFeB, and their high stability benefits the thermal budget during the back-end-of-line process [139,140]. Moreover, field-free switching techniques need to be compatible with wafer-scale growth and nanofabrication. Furthermore, to reduce switching current density and enhance cell selectivity, voltage-gate assisted SOT has been proposed, a topic to be discussed in the next section.

### 3.2. Voltage-controlled magnetic anisotropy

The voltage-controlled magnetic anisotropy (VCMA) effect has been highlighted as the scheme to control the magnetization with extremely low power consumption since it is driven by electric field without any additional electrical current. Among the phenomena with various origins, most of the interest towards the use in the application is on the electronic effect based on the electron depletion and accumulation at the interface between the ferromagnetic and dielectric layers, depending on the polarity of the electric field [141–143]. The changes in the hybridized orbitals close to the interface consequently modulate the interfacial magnetic anisotropy originating from the spin–orbit interaction as shown in Figure 7(a), an example change of charge density induced at $\pm 0.2$ V/nm electric fields in the MgO [144].

VCMA effect changes anisotropy energy and consequently modifies the energy landscape of the magnetization. The example of VCMA effect reflected in the change in coercivity of MTJ device is shown in Figure 7(b). Eventually, sufficiently strong VCMA effect can change the direction of the minimum magnetic energy [145,146]. Such impact by VCAM effect allows the switching of magnetization back and forth with voltage pulses, combined with the external magnetic field orthogonal to the easy axis direction at zero bias

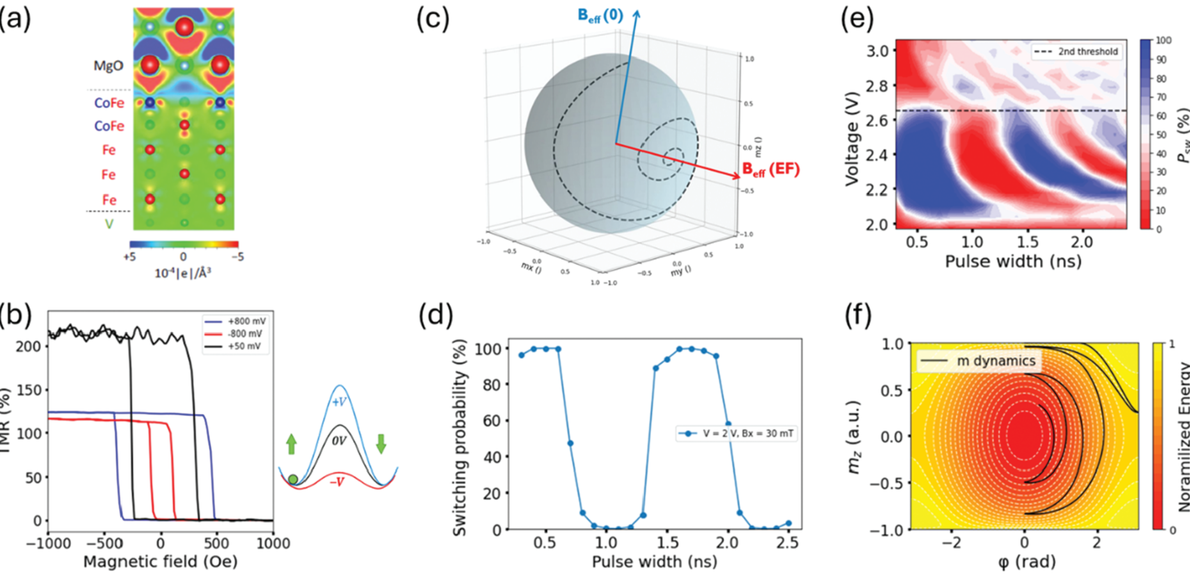


Figure 7. (a) Computational model with the induced change of charge density at $\pm 0.2$ V/nm electric fields in the MgO. The blue and red areas represent the hole accumulation and depletion, respectively [144]. (b) VCMA effect reflected in the TMR with schematics of energy barriers on the right [151]. (c) Precession trajectory from the initial direction at zero bias ($B_{eff}(0)$) to the final direction at applied electric field ($B_{eff}(EF)$) (d) switching probability experiments with various pulse width [151]. (e) Switching probability calculation in contour for various pulse voltage and width. Dotted line indicates the second threshold in switching probability [151]. (f) Magnetization precession in the energy landscape at the voltage above the second threshold in (e). Y-axis is $m_z$ component and x-axis is the azimuthal angle [151].

from in-plane MTJ [147] and perpendicular MTJ [148] devices. Standalone VCMA-driven switching exploits the precession of the magnetization around the direction of the external field, due to the abrupt change in the energy landscape by the voltage pulse. Figure 7(c) visualizes an example trajectory of the free layer magnetization with macrospin assumption when the direction of the effective magnetic field is changed from $B_{\mathrm{eff}}(0)$ to $B_{\mathrm{eff}}(\mathrm{EF})$ by VCMA effect. If we tune the pulse width to turn off when the magnetization is in the direction close to the opposite direction to the initial direction, for example, after the half of the precession period, the magnetization becomes switched as it stabilizes to the reverted easy axis but in the opposite direction. The precessional characteristics are clearly reflected in the oscillatory probability of the switching depending on the pulse width as in Figure 7(d). The dependence of the amplitude and width of the pulses have been investigated on various parameters with analytical models and experiments [145,146,149,150]. Furthermore, a break in the switching regime in the switching probability diagram was observed both in experiment and in macrospin model analysis (Figure 7(e)) where $p$ parameter represents the amplitude of the VCMA effect, defined as the reduction in the anisotropy field ($H_{\mathrm{K}}$) normalized by $H_{\mathrm{K}}$ at zero bias. It reflects the additional precession around the initial direction as it becomes the hard axis with maximum energy by the strong VCMA effect above the threshold, as in Figure 7(f) [151].

Perpendicular MTJ devices attract more interest since they can provide sufficient data retention for the memory application. The VCMA-induced precessional write scheme shows the potential of the sub-ns speed in addition to the advantage of low power consumption suppressing the current flow in the write operation. However, important challenges need to be solved to take advantage for the application. The orthogonal field to induce the precession requires additional solutions for the operation in the integrated structure. There have been studies such as the field-free operation solution using conically magnetized free layer [152] and the in-plane magnet integrated on top of the MTJ pillar [153]. The offset field of the free layer must be controlled precisely for the symmetry in the energy barriers of P and AP states and consistent write operation with the identical pulses as a result [154]. Since the two switching directions share the same pulse, if the device is already in the wanted state, we should not send the write pulse. It means we need to read the device prior to the application of the write pulse and need to decide whether to send it or not since the write pulse is not deterministic. The solution for the deterministic switching is proposed to induce the asymmetry in the energy barrier by intentional offset field and design the different write pulses for the two directions [153]. Suppression of the write error rate has been investigated because impact of the stochasticity can be significant since it uses even less than one period of the precession [155–157].

Along with all the challenges in the operation characteristics, the essential challenge is the enhancement of the VCMA effect. To write the memory device with high retention and high energy barrier, the stronger VCMA effect is necessary. However, the write voltage is limited by the dielectric breakdown of the tunnelling barrier [158]. Therefore, we need higher efficiency of VCMA effect to allow stronger VCMA effect with given voltage. The efficiency of VCMA effect is generally represented by the VCMA coefficient, the slope from the linear dependence of the interfacial anisotropy energy on the applied electric field, with the unit of J/Vm [145,159,160]. Requirement of the VCMA coefficient for the application is estimated to be a few hundred or higher [161]. Design of MTJ stack has been studied experimentally with the assist of the atomistic models, engineering the interface with doping heavy metals [162,163] and using various metals in the adjacent layers to the ferromagnetic layer [164]. While dielectric materials with high dielectric constant like $HfO_x$ and $SrTiO_x$ were also investigated [160,165,166], but MTJs with MgO layer with Co- or Fe-based ferromagnetic layers attract more interest for the application since they can provide large TMR ratio for read signal. Large VCMA coefficient of 300 fJ/V-m achieved from MBE-deposited Fe/MgO MTJ [159] and the VCMA coefficients beyond 100 fJ/V-m achieved from sputtered pMTJ pillar devices with help of atomistic simulation for insertion materials at the interface of MgO/CoFeB [163].

While various advantages and challenges are still open to being the alternative standalone write scheme for MRAM, VCMA effect has been also studied for the switching combined with STT effect [167,168] and can provide the selectivity in the configuration of multiple MTJs on top of a heavy metal line for SOT effect [169]. Moreover, while various spintronic schemes are potential candidates, the benefit of low power operation is still valid for VCMA effect, to be used for the application beyond the memory device, like physically unclonable functions and random number generators [170,171].

### 3.3. Orbitronics

Electrons in solids possess both spin angular momentum (SAM) and orbital angular momentum (OAM). While SAM manipulation has been extensively studied through mechanisms like the spin-filter effect, SHE, and REE, OAM manipulation was historically overlooked due to the belief that OAM was quenched in equilibrium by crystalline field. However, recent theoretical studies suggest that non-equilibrium OAM can be driven by external fields. Specifically, theories concerning the SHE in 4d and 5d transition metals indicated that the orbital Hall effect (OHE) is the origin of their giant SHE [113,114]. Later, it was predicted that non-equilibrium OAM can be generated even without SOC. With broken inversion symmetry, the orbital Rashba coupling – a momentum-dependent OAM expectation value – was theorized [172]. An external electric field, combined with orbital Rashba coupling, could then enable orbital polarization via the orbital Rashba-Edelstein effect (OREE) [173–175]. In materials with inversion symmetry, an external electric field induces a transverse OAM current, leading to the orbital Hall effect (OHE) [176,177]. Theoretical calculations suggest high orbital conductivity, a few $10^3$ $(\hbar/e)\ \Omega^{-1}\ \mathrm{cm}^{-1}$, across a wide range of nonmagnetic metals [178]. Notably, light metals (LMs) with weak SOC, such as Ti, V, Cr, and Mn, are expected to exhibit dominant OAM generation over SAM generation due to their large orbital Hall conductivity and negligible spin Hall conductivity.

An orbital current flowing into a ferromagnet can induce torque on its magnetization, a process mediated by orbital-to-spin conversion [179]. This mechanism was crucial for initial experimental confirmation of OAM generation and transport. Researchers applied established SOT measurement techniques (ST-FMR, HHV, and MOKE) to various light metal/ferromagnet (LM/FM) heterostructures, including LMs such as Cu, Cr, Mn, Ti, Nb, Ru, and Zr [180–188]. Despite the weak spin-orbit coupling (SOC) in LMs, a significant torque on the FM was observed, compellingly attributed to orbital generation within the LM via OREE or OHE. Intriguingly, even in high-SOC materials like Ta, W, and Pt, where spin Hall conductivity is comparable to orbital Hall conductivity, evidence of orbital torque was revealed [183,185,186]. When both spin and orbital currents contribute to the total torque, its combined effect can be described by [183],

$$\mathrm{SOT} = T_S J_S + \eta_{SL} T_L J_L, \quad (4)$$

where $J_S/J_L$ is the spin/orbital current from LM, $T_S/T_L$ is the spin/orbital transmission at the LM/FM interface, and $\eta_{SL}$ is the orbital-to-spin conversion efficiency of FM. It is noteworthy that the magnitudes and signs of $J_S$ and $J_L$ are governed by the spin Hall and orbital Hall conductivities, respectively. The necessity of the orbital-to-spin conversion ($\eta_{SL}$) process arises because OAM itself does not directly exert torque on FM magnetization, and its efficiency is highly dependent on the specific FM material (Figure 8(a)). For instance, the SOT sign for NM/Ni (where NM is Cr, Mn, or Ta) is inverted compared to NM/Co and NM/Fe, a phenomenon explained by the strong $\eta_{SL}$ of Ni [183–185]. This result cannot be explained by spin torque because the material-dependent $T_S$ only affects SOT magnitude for a given $J_S$. To further enhance orbital torque efficiency, trilayer structures of LM/HM/FM were investigated. The insertion of a heavy metal (HM) such as Pt, Gd, or Tb was found to act as an efficient orbital-to-spin conversion layer, leading to high SOT efficiencies exceeding 0.2 [185,189,190].

Spin pumping, the generation of spin current from a ferromagnet (FM) to a non-magnet (NM) driven by magnetization precession, is the reciprocal of spin torque [193]. Similarly, orbital pumping, defined as the magnetization-precession-driven orbital current flowing from FM to NM, is theorized as the reciprocal process of orbital torque. This orbital-pumped orbital current can be electrically detected via orbital-to-charge conversion mechanisms, specifically the inverse OHE or inverse OREE [191]. To isolate the orbital signal and suppress spin-related contributions from inverse SHE or inverse SREE, experiments have employed materials with weak spin-orbit coupling (SOC), such as Ti [191]. A key experimental signature confirming orbital pumping is its strong dependence on the FM material: significant orbital pumping was observed in Ni/Ti bilayers, but it was negligible in Fe/Ti bilayers (Figure 8(b)). Given that OAM does not directly couple with magnetization, orbital pumping inherently requires spin-to-orbital conversion. In addition to orbital pumping, orbital currents have been generated through thermally driven process of spin Seebeck effect [[194]] and optically driven process of ultrafast demagnetization [195].

Both orbital torque and orbital pumping rely on the orbital-spin conversion occurring within a ferromagnet. To detect the initial orbital generation processes of OHE and OREE in light metals (LMs) without the

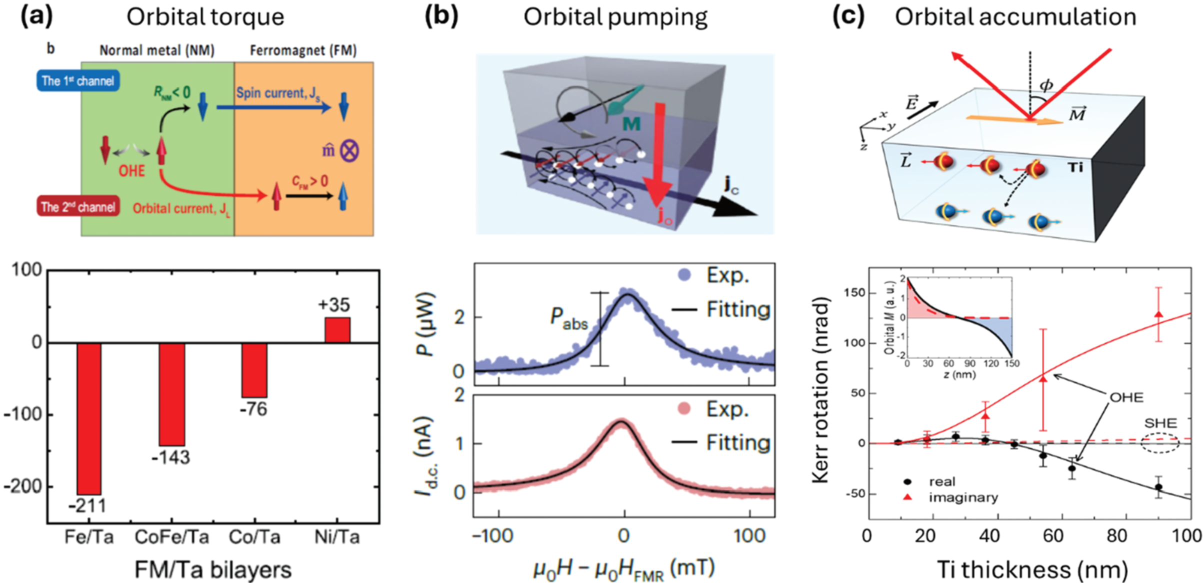


Figure 8. Experiment observation of orbitronics. (a) Orbital torque in the Ta/ferromagnet bilayer. Spin-orbit torque efficiency critically depends on ferromagnet materials. The figure is reproduced with permission from ref [183]. (b) Orbital pumping in the Ti/Ni bilayer. Spin pumping produces a transverse charge current ($J_C$) at ferromagnetic resonance. The figure is reproduced with permission from ref [191]. (c) Orbital accumulation in the Ti single layer. Magneto-optical Kerr effect detects orbital magnetization on Ti surface. The figure is reproduced with permission from ref [192].

involvement of a ferromagnet, researchers have successfully used optical detection of orbital accumulation in single layers of LMs, including Ti, Cr, and V [192,196,197]. When an orbital current flows within an LM, it leads to orbital accumulation at the material's boundaries, which can then be detected using the magneto-optical Kerr effect (MOKE). To differentiate between orbital and spin accumulation, the relative sensitivity of the optical measurement to each type of magnetization is critical. When both SHE and OHE contribute to spin and orbital accumulation, the Kerr rotation can be expressed as [192,]:

$$\tilde{\theta}_{\mathrm{K}}\left(d_{\mathrm{NM}}\right)=O_{\mathrm{L}}\int_{0}^{d_{\mathrm{NM}}}M_{\mathrm{L}}\left(z\right)\kappa e^{-\kappa z}dz+O_{\mathrm{S}}\int_{0}^{d_{\mathrm{NM}}}M_{\mathrm{S}}\left(z\right)\kappa e^{-\kappa z}dz. \tag{5}$$

Here, $O_{\mathrm{L}}$ and $O_{\mathrm{S}}$ represent the optical sensitivity for uniform orbital and spin magnetization, respectively, while $M_{\mathrm{L}}$ and $M_{\mathrm{S}}$ denote the orbital and spin accumulation. The parameter $\kappa$ accounts for the light penetration effect, which is determined by the light's wavelength and the refractive index of the nonmagnetic material, and $z$ is the distance from the top surface. In LMs with weak SOC, both the spin sensitivity ($O_{\mathrm{S}}$) and spin accumulation ($M_{\mathrm{S}}$) are significantly suppressed, causing the Kerr rotation to be dominated by the orbital contribution. For a quantitative analysis of the Kerr rotation, both the orbital sensitivity ($O_{\mathrm{L}}$) and orbital accumulation ($M_{\mathrm{L}}$) must be determined. The $O_{\mathrm{L}}$ can be obtained from independent measurements of the Oersted-field-driven orbital induction [192,]. The $M_{\mathrm{L}}$ is governed by the orbital generation term (orbital Hall conductivity) and the orbital relaxation term (orbital relaxation time and orbital diffusion length) (Figure 8(c)).

The electrical manipulation of non-equilibrium orbital states has been successfully demonstrated through recent research on orbital generation in nonmagnetic materials and orbital torque and pumping in nonmagnet/ferromagnet bilayers. Inserting an orbital-to-spin conversion layer, the efficiency of orbital torque from LM can be comparable to that of spin-orbit torque from HM (Table 4). Future applications necessitate the development of more efficient orbital generation and orbital-to-spin conversion, achievable through innovative material designs and device architectures. Beyond non-equilibrium states, this electrical manipulation technique holds potential for controlling equilibrium orbitals, which are profoundly impactful on magnetic properties. For example, orbitals are the direct link between a material's anisotropic crystal structure and its magnetization, defining magnetic anisotropy energy. Furthermore, in epitaxial or textured magnetic tunnel

**Table 4.** Summary of efficiency of orbital torque ($\theta_{eff}$), which is a combined process of orbital generation in nonmagnet (NM), orbital-to-spin conversion, and spin torque in ferromagnet. $\rho_{NM}$ is the electrical resistivity of the orbital generation layer of NM. The orbital generation mechanism can be classified to the bulk effect of orbital Hall effect (OHE) and interfacial effect of orbital Rashba-Edelstein effect (OREE).

| Class | Structure | Method | $\lvert\theta_{eff}\rvert$ | $\rho_{NM}$ (μΩ cm) | Ref. |
|---|---|---|---|---|---|
| OHE from NM | Ta/Ni | ST-FMR | 0.03 | 200 μΩ cm | [183] |
| | Ti/Ni | ST-FRM, MOKE | 0.02 | 60 μΩ cm | [186,] |
| | Cr/Ni | HHV | 0.015 | 360 μΩ cm | [184] |
| | Nb/Ni | ST-FMR | 0.018 | 41 μΩ cm | [187,] |
| | Ru/Ni | ST-FMR | 0.019 | 27 μΩ cm | [187,] |
| | Zr/Ni | ST-FMR | 0.02 | 53 μΩ cm | [188,] |
| OHE from NM + conversion layer | Cr/Gd/Co | HHV | 0.25 | 56 μΩ cm | [185] |
| | Cr/Tb/Co | HHV | 0.23 | 56 μΩ cm | [185] |
| | Ru/Pt/[Co/Ni] | HHV | 0.47 | 50 μΩ cm | [190,] |
| | Zr/[Co/Pt] | HHV | 0.78 | 770 μΩ cm | [189] |
| OREE from interface | CuOx/Cu/NiFe | ST-FMR | 0.08 | | [180] |
| | Al2O3/Cu/CoFe | ST-FMR | 0.13 | | [182] |

junctions (MTJs), orbital symmetry critically determines tunneling conductance. Therefore, gaining efficient control over orbital symmetry could enable novel functionalities across diverse magnetic phenomena.

### 3.4. *Antiferromagnetic spintronics*

Antiferromagnets present significantly broader material choices, encompassing metals, insulators, and semiconductors, when compared to ferromagnets [198–200]. Traditionally, their absence of net magnetization restricted their use in memory devices to passive roles, such as providing exchange coupling for pinned layers. However, a growing interest has recently emerged in leveraging antiferromagnets as active information storage media [198–200]. Antiferromagnets have several advantages over ferromagnets; they exhibit strong robustness against external magnetic field perturbations, thereby reducing crosstalk between memory cells, and possess much higher resonant frequencies, enabling exceptionally fast operation speeds. Realizing antiferromagnet-based memory applications critically depends on establishing efficient mechanisms for both reading and writing of the antiferromagnetic order.

Conventionally, electrical reading of antiferromagnetic orders relied on AMR [201–203]. While high tunnel AMR, exceeding 100% at low temperatures, was observed in IrMn/MgO/Pt structures [201,202], its low room-temperature magnitude and insensitivity to magnetization reversal (AMR is even on magnetization) presented limitations. Furthermore, AMR-based reading of collinear antiferromagnets necessitates multi-terminal structures (four or eight terminals), making them susceptible to thermal artifacts from anisotropic thermal gradients and voltages [204].

A breakthrough emerged with the discovery of a magnetization-odd anomalous Hall effect (AHE) in non-collinear chiral antiferromagnets like $Mn_3X$ (X = Sn, Ge, Ga, Ir, Pt, Rh) [205–212]. In these materials, Mn atoms form a kagome lattice with a fixed chiral, triangular magnetic moment configuration. This chiral spin structure enables non-vanishing Berry curvature in momentum space, leading to large topological magneto-transport responses, including AHE [205–212], anomalous Nernst effect [213], and magneto-optical Kerr effect [214]. The magnetic octupole moment, acting as the collective magnetic order parameter, determines the AHE sign. Remarkably, the magnitude of AHE in several non-collinear antiferromagnets rivals that of ferromagnets at room temperature [205–212]. However, AHE is not desirable for memory reading mechanism due to low magnetic signal from AHE and large nonmagnetic signal from a leakage current in four-terminal Hall-bar structures.

More recently, TMR in two-terminal MTJ devices with non-collinear chiral antiferromagnets has been reported [215–217]. Here, the tunnel conductance of antiferromagnet/barrier/antiferromagnet junctions depends on the parallel and antiparallel alignments of antiferromagnetic ordering vectors. Epitaxial $Mn_3Pt/MgO/Mn_3Pt$ and polycrystalline $Mn_3Pt/Al_2O_3/Mn_3Pt$ junctions exhibited high TMR exceeding 100% at room temperature [215,217], whereas an epitaxial $Mn_3Sn/MgO/Mn_3Sn$ junction showed a comparatively lower TMR of 2% [216]. The underlying mechanism has been attributed to spin-polarized current or momentum-dependent spin polarization within the chiral antiferromagnet [218,219]. Such a large magnetic signal in a two-terminal device is ideal for memory reading operation.

Switching antiferromagnetic order presents a significant challenge. It was initially believed that conventional STT or SOT, effective for ferromagnets, would not apply to antiferromagnets due to their lack of net magnetization. However, a new type of spin torque was discovered in single layers of CuMnAs and $Mn_2Au$, where spin sublattices form space-inversion partners [220–222]. Although the full crystal lattices of CuMnAs and $Mn_2Au$ are inversion symmetric, each Mn sublattice exhibits broken inversion symmetry. Consequently, a charge current locally generates non-equilibrium spin density with opposite signs on these inversion-partner Mn sublattices via REE (or inverse spin galvanic effect). The combination of these oppositely signed current-driven spins and local Mn moments at the two sublattices results in a finite torque on the antiferromagnetic order, specifically the Néel vector [220–222] (Figure 9(a)). A limitation of this 'Néel SOT' is its propensity for 90° switching, where the antiferromagnetic order aligns perpendicular to the applied current.

Bidirectional 180° switching of antiferromagnetic order was subsequently achieved in heterostructures of heavy metals (Pt or W) and non-collinear chiral antiferromagnets ($Mn_3Sn$) [223–230]. When spin current is injected from the heavy metal *via* SHE, the switching protocol for the antiferromagnet is the same as that of a ferromagnet: the sign of the heavy metal's SHE and a symmetry-breaking external field determined the switching direction of the antiferromagnetic order (Figure 9(b)). Initially, with six-fold anisotropy in the Kagome plane, 30% partial switching (compared to magnetic-field-driven full switching) was observed [223]. Later, 100% full switching was attained by inducing two-fold anisotropy with an in-plane tensile stress [224]. These results suggest that spin current can be absorbed by the antiferromagnetic order of chiral antiferromagnets, thereby inducing torque.

SOT on antiferromagnets also exhibits unique properties distinct from SOT on ferromagnets, including chiral spin rotation, heating effect, handedness anomaly, and long spin coherence length. Above a certain threshold, SOT can induce a continuous rotation of the magnetic moment within the Kagome plane (chiral spin rotation). Experimental evidence for this chiral spin rotation included characteristic fluctuations of the Hall resistance arising from the spatial average of domain configurations and local stray fields from nanoscale domains [225,226]. SOT-driven switching critically relies on Joule heating near the Néel temperature of the antiferromagnet, with the spin current setting the domain configuration during cooling (heating effect) [227,228]. Furthermore, SOT rotates the octupole moment of chiral antiferromagnets in the opposite

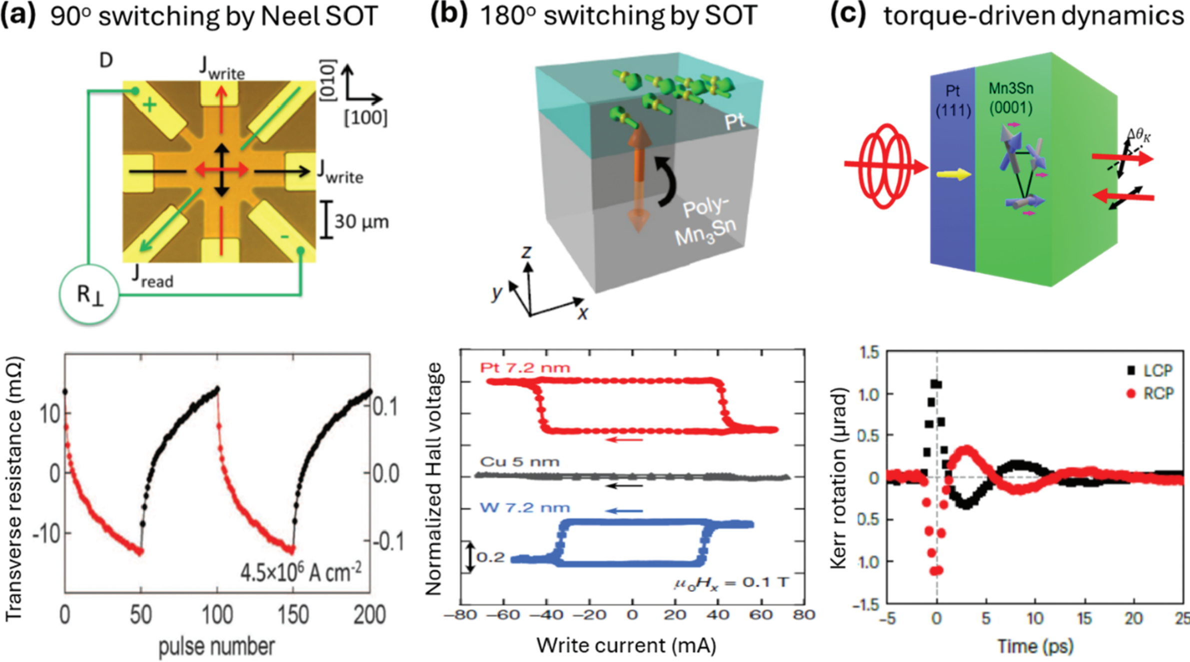


**Figure 9.** Writing and reading of antiferromagnetic orders. (a) 90° switching of CuMnAs driven by Neel spin-orbit torque and reading by anisotropic magnetoresistance of CuMnAs. The figure is reproduced with permission from ref [220]. (b) 180° switching of $Mn_3Sn$ driven by spin-orbit torque from Pt and reading by anomalous Hall effect of $Mn_3Sn$. The figure is reproduced with permission from ref [223]. (c) 70 GHz precessional dynamics of $Mn_3Sn$ driven by ultrafast spin current. The spin current is generated by optical spin orientation in Pt. The figure is reproduced with permission from ref [230].

direction to individual moments (handedness anomaly) [229]. The spin coherence length, representing the distance over which a transverse spin current is absorbed by magnetization, was found to be much longer in $Mn_3Sn$ (15 nm) than in conventional ferromagnets (<1 nm) [230]. Time-resolved measurements of spin torque on chiral antiferromagnet $Mn_3Sn$, employing optical spin generation in the HM, further revealed that spin current injection leads to immediate damping-like torque and induces precessional dynamics perpendicular to the Kagome plane with a high resonance frequency of 70 GHz (Figure 9(c)) [230], which could enable fast writing operations for memory devices.

Recent breakthroughs in reading and writing antiferromagnetic order have demonstrated their potential as information carriers. To fully realize antiferromagnetic spintronics, significant enhancements are required for both reading and writing capabilities. For fast and reliable reading, a TMR exceeding 200% with a narrow distribution is necessary. To offer a distinct advantage over ferromagnets, deterministic switching of antiferromagnets at the picosecond timescale is crucial. Furthermore, strong perpendicular magnetic anisotropy and a high Néel temperature are beneficial for ensuring thermal stability at small sizes and achieving long-term data retention in memory cells. Finally, for large wafer-scale integration of memory cells, it is essential to achieve the desired crystal structure of antiferromagnets on silicon substrates, as this is critical for their reading, writing, and thermal stability properties.

## 4. New applications of spintronics

### 4.1. Spin torque oscillators

Spin torque oscillators (STOs) have attracted significant interest for applications in wireless communication [231–233], data storage [234,235], and neuromorphic computing [236–238]. The operational principle of STOs relies on spin-transfer torque (STT) [68] and spin-orbit torque (SOT) [239], where a spin-polarized current induces sustained precessional dynamics within a ferromagnetic layer. This precessional motion is then converted into an electrical signal through magnetoresistive effects, such as GMR, TMR, and AMR, forming the basis of spin torque nano-oscillators (STNOs) and spin Hall nano-oscillators (SHNOs). STOs exhibit tunable frequencies spanning from MHz to tens of GHz, with the potential to extend into the sub-THz regime [240–243], possess nanoscale dimensions, and display rich nonlinear dynamics. Key performance metrics, including linewidth, output power, and threshold current, remain central to ongoing optimization efforts, with synchronization emerging as a promising strategy for enhancing signal coherence and power output.

Advances in nanofabrication techniques have facilitated the development of STOs with nanoscopic dimensions, thereby reducing the current requirements. Different STNO architectures have been developed and illustrated in Figure 10. Early STNO designs utilized mechanical point contacts (Figure 10(a)) [67]), which were subsequently replaced by lithographically defined nano-contact (Figure 10(b)) [244,245]) or nano-pillar structures (Figure 10(c)) [68]). Nano-contact STNOs confine current injection to a nanoscale region on an extended film, enabling nonlinear magnetization dynamics such as spin waves [246], localized bullet [247], and magnetic droplets [248–250], which are particularly in systems exhibiting perpendicular magnetic anisotropy (PMA). In contrast, nano-pillar STNOs involve patterning the entire multilayer structure, requiring lower current densities for STT-induced oscillations but typically exhibiting larger linewidths due to their smaller magnetic volumes. Nano-pillar STNOs based on magnetic tunnel junctions (MTJs) often feature sub-100 nm pillars with perpendicular current flow [251–253]. MTJs offer higher TMR ratios compared to GMR, leading to enhanced output power, although their fabrication can be more complex.

SHNOs represent another class of STT-driven oscillators that utilize an in-plane charge current in a heavy metal (HM) layer with strong spin-orbit coupling to generate a perpendicular pure spin current via the spin Hall effect (SHE) [239,254,255]. This spin current then induces magnetization oscillations in an adjacent ferromagnetic (FM) layer through SOT. SHNOs offer advantages such as simpler fabrication and integration potential due to in-plane current injection and can operate in FM/HM bilayer configurations. Readout via AMR in the FM layer typically results in lower output power compared to TMR-based STNOs but allows for innovative designs like coupled oscillator arrays [255–258]. The advent of SHNOs broadens the STT oscillator paradigm, providing new design flexibilities linked to the fundamental understanding and engineering of the SHE, thus expanding the landscape of spintronic oscillator design (Figure 10(d–f)). The selection of appropriate STO architecture necessitates careful consideration of fabrication complexity, output power

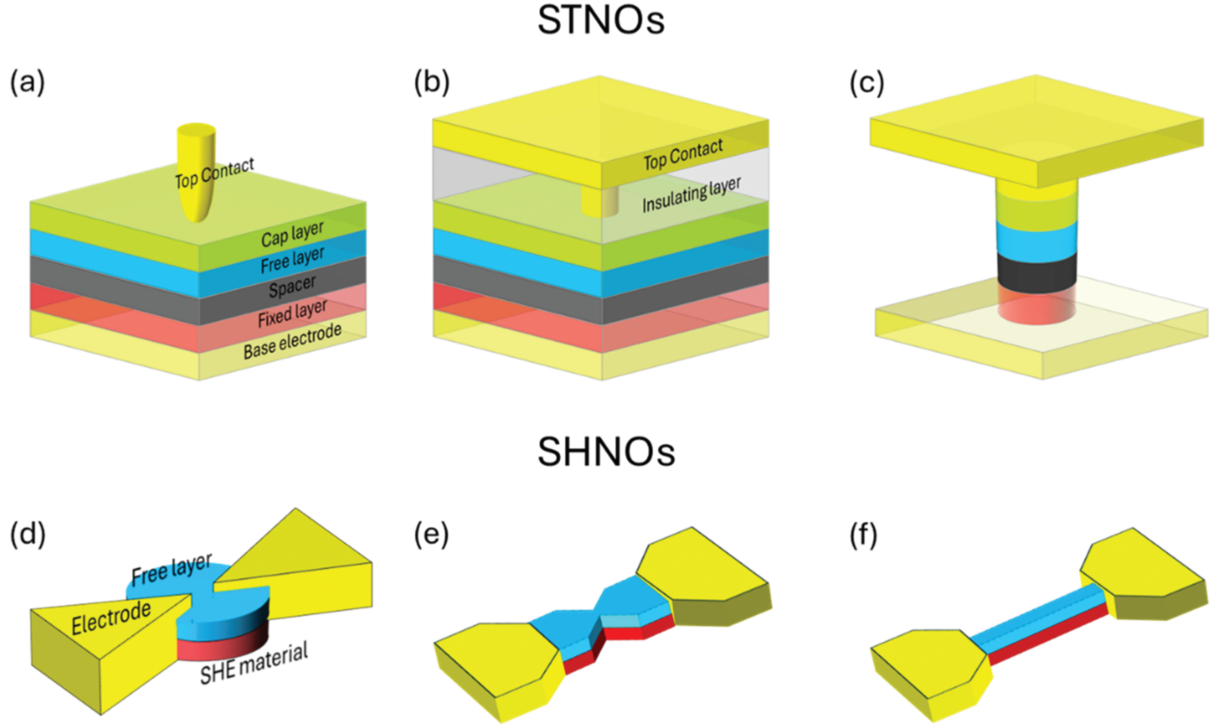


**Figure 10.** Device architectures and geometries of STNOs (top) and SHNOs (bottom). Layers are color-coded as shown in (a) for STNOs and (d) for SHNOs. Featured device geometries include the following: (a) point-contact, (b) nano-contact, (c) nano-pillar, (d) nano-gap, (e) nano-constriction, and (f) nano-wire.

requirements, and specific application demands, reflecting the continuous advancement and diversification within STO technologies.

The choice of materials and the configuration of magnetic layers are crucial factors determining the performance characteristics of STOs. While conventional materials like NiFe and CoFeB offer tunable anisotropy and low damping properties, more sophisticated material systems, including synthetic antiferromagnets (SAFs) [243], Heusler alloys (e.g. CoFeMnSi) [259–261], and high-anisotropy multilayers (e.g. Co/Pt) [66,262], contribute to improved stability and output power. Furthermore, innovative device designs, such as sombrero structures and SHNOs, enhance the efficiency of spin current generation and utilization. The relative magnetization orientation between the free and fixed magnetic layers significantly impacts STO characteristics [247–250,263]. Specifically, tilted anisotropy configurations, often achieved through the implementation of exchange-spring magnets [263], enable field-free operation and enhanced frequency tunability. Performance optimization is typically achieved by strategically pairing soft magnetic materials (e.g. NiFe) for the free layer with hard magnetic materials (e.g. SAFs) for the fixed layer. Recent research has increasingly focused on the utilization of perpendicular magnetic anisotropy (PMA) materials and heavy metal layers (e.g. Ta and W) to achieve higher output power and lower critical current densities. The mutual synchronization of STOs, facilitated by spin-wave coupling [244,245,255–257], electrical coupling [236,237,264], and magneto-dipolar interactions [265,266], has emerged as a significant mechanism for enhancing collective signal output and spectral coherence. In synchronized arrays, the constructive interference of individual oscillators leads to a substantial increase in microwave emission power and a considerable narrowing of linewidth. These improvements are not only critical for conventional high-frequency applications such as wireless communications but also for unconventional computational paradigms rooted in neuromorphic engineering.

In neuromorphic computing, which aims to emulate the structural and functional principles of biological neural systems, the nonlinear and tunable dynamics of STOs offer a compelling platform for implementing artificial neurons [236–238]. Their intrinsic threshold behavior, frequency agility, and capability to synchronize in complex patterns allow for the realization of biologically inspired computational features, including spiking

behavior, phase-based information encoding, and emergent synchronization. Networks of mutually synchronized STNOs have demonstrated functionalities such as associative memory and pattern recognition, with phase relationships serving as carriers of encoded information. SHNOs, benefiting from more scalable fabrication and voltage-controlled frequency modulation [256,267], further enhance the prospects of large-scale neuromorphic hardware. Mechanisms such as voltage-controlled magnetic anisotropy (VCMA) enable dynamic frequency tuning, potentially mimicking synaptic plasticity and allowing for in situ reconfiguration of network behavior. The multifunctionality of spintronic elements – where magnetic tunnel junctions (MTJs) act as non-volatile synapses and STNOs/SHNOs serve as dynamic neurons – supports the construction of densely integrated, low-power, event-driven computational architectures.

Recent studies have demonstrated neuromorphic tasks, such as spoken digit recognition [237,238], using multiple STNO or SHNO arrays in a reservoir computing framework. As these arrays increase in scale, the challenge becomes ensuring uniform synchronization, managing device variability, and achieving robust coupling under fabrication constraints. STNO/SHNO-based networks might offer more than an alternative to conventional CMOS-based AI hardware; they represent a fundamentally distinct computational approach – often referred to as an Ising machine – which has been receiving significant attention [268–271]. By leveraging the rich physics of nonlinear magnetization dynamics, spintronic neuromorphic systems may enable adaptive, real-time processing architectures uniquely suited to sensory-driven tasks in compact, energy-efficient formats.

Despite significant advancements in STOs, several key challenges hinder their widespread commercialization. These include achieving consistent high-power output with ultra-narrow linewidth across devices, reducing performance variability, and enhancing device reliability and operational lifetime. Future research endeavors are crucial for exploring novel materials capable of terahertz-range oscillations and exhibiting enhanced spin-orbit coupling, optimizing device geometries, and advancing synchronization techniques for oscillator networks. Integrating STOs with CMOS circuitry remains a significant focus, necessitating alignment of fabrication processes and operating conditions. The exploration of antiferromagnetic and ferrimagnetic systems presents potential pathways toward terahertz operation regimes. While current limitations such as low output power and high phase noise persist, on-going research into innovative materials and device designs promises to overcome these hurdles. STOs, with their nanoscale dimensions and frequency tunability, hold considerable potential to revolutionize microwave electronics, neuromorphic computing, and sensing applications within next-generation electronic devices.

### *4.2. MTJ-based probabilistic computing*

Classical von Neumann computing systems excel at arithmetic and bitwise logic but struggle with problems that lack concise deterministic formulations, particularly NP-class combinatorial optimizations, such as factoring, protein folding or traveling-salesman problem. The complexity of these problems increases exponentially with problem size, making it impossible for existing systems to provide optimal solutions in a practical amount of time. On the other hand, an Ising machine could provide a tractable solution framework by mapping any NP problem onto a network of spins ($\pm 1$), with the coupling strengths encoding the problem's constraints [272,273]. According to the Boltzmann thermodynamic theory, an ensemble of interacting spins at thermal equilibrium spends the majority of its time in low-energy configurations. By expressing a given problem as a Hamiltonian (energy-cost) function, the system naturally relaxes toward minimal-energy spin states; the most probable observed state then corresponds to the optimal – or a near-optimal – solution [274]. Direct implementation of this mapping in a specialized hardware offers a path to efficiently approximate or solve such intractable tasks.

Probabilistic computing is a special form of Ising-machine-inspired analog-digital hybrid scheme in which each node is a probabilistic bit (P-bit) rather than a fixed $\pm 1$ spin [275]. Unlike a conventional bistable memory cell, an unbiased P-bit (analog input $I = 0$) fluctuates between its two states (–1 and +1) with equal likelihood under thermal activation (Figure 11(a)). When a nonzero analog signal ($I \neq 0$) is applied, the P-bit's stochastic oscillations become biased toward one state, so that its instantaneous output ($m$) follows $m = \text{sgn}[\tanh(I) + r]$, where $\text{sgn}[\cdot]$ yields $\pm 1$ and $r$ is a uniform random variable in (–1, +1). By adjusting each P-bit's input $I$, one controls the average value of its binary random output, enabling

controlled probabilistic behavior. In probabilistic computing, network of P-bits performs computation by encoding the problem Hamiltonian directly into their weighted interconnections [273]. Although P-bit's and weight's updates resemble those used in artificial-neural-network training, their role here is to reshape each P-bit's probability distribution in accordance with the problem's energy function (Figure 11(b)). Every P-bit simultaneously receives signals from – and sends signals to – its connected ones, so that the output of one device influences the fluctuations of others. The network's weight matrix is derived from the target Hamiltonian: one may implement a symmetric Hopfield or Boltzmann-machine topology or a directed Bayesian-network structure and then apply stochastic-annealing or neural-inference algorithms to drive the system toward low-energy configurations, enabling both optimization and inverse logic operations (Figure 11(c)).

A possible P-bit source includes pseudorandom generator – such as linear-feedback shift registers and ring oscillators – in digital CMOS, which allow rapid prototyping but lack true randomness and demand substantial area and power (>1000 –5000 transistors per P-bit). Other physical systems exhibit stochastic switching suitable for P-bits: Johnson–Nyquist thermal noise, ring-oscillator phase jitter, threshold switching ReRAM, phase-change materials, Mott insulator–metal transitions, ovonic threshold switches, nonlinear oscillators, and 2D-FETs. Each platform brings its own trade-offs in device complexity, reproducibility, and large-scale integration. Among the various P-bit platforms, stochastic magnetic-tunnel junctions (MTJs) have emerged as the frontrunner [276–278]. In MRAM, MTJs are engineered for a high thermal-stability factor ($\Delta_0 = E_b/k_B T > 60$) to retain data for over 10 years. By contrast, lowering $\Delta_0$ to ~10 induces microsecond-scale spontaneous flips (Figure 11(a)), and further down to 1–2 yields nanosecond-scale fluctuations [279,280]. Applying a spin-polarized current modulates the effective energy barriers for state transitions, thereby controlling each P-bit's bias. Peripheral CMOS circuitry, consisting of transistor, resistor, comparator, then converts analog inputs into the device's stochastic digital outputs. Because it exploits intrinsic nanoscale randomness for ultra-low-power operation and reuses mature MTJ technology in standard MRAM foundries [281], the approach holds great practical promise.

Since its proposal in 2017, probabilistic computing has progressed rapidly. In 2019, Purdue University and Tohoku University demonstrated stochastic STT-MTJ-based P-bit hardware capable of factoring three-digit composites, validating the concept at the device level [282]. In 2022, University of California, Santa Babara team implemented a P-bit computer on FPGA to factor 32-bit composites [283]. And in 2024, a group at the National University of Singapore used an 80-device STT-MTJ array to solve instances of the traveling-salesman problem [284], a canonical NP-hard task. Follow-on studies have since expanded to diverse emerging devices [285–287] including SOT-MTJ, ReRAM, phase-change elements, nonlinear oscillators, 2D materials, underscoring the field's rapid evolution and growing versatility. Unlike emerging device-based P-bit implementations, synaptic networks of probabilistic computers have so far been emulated on digital MCUs or FPGAs [288]. Since many of their compute kernels ultimately reduce to matrix–vector multiplications – just like neural networks – researchers are now exploring analog-CMOS

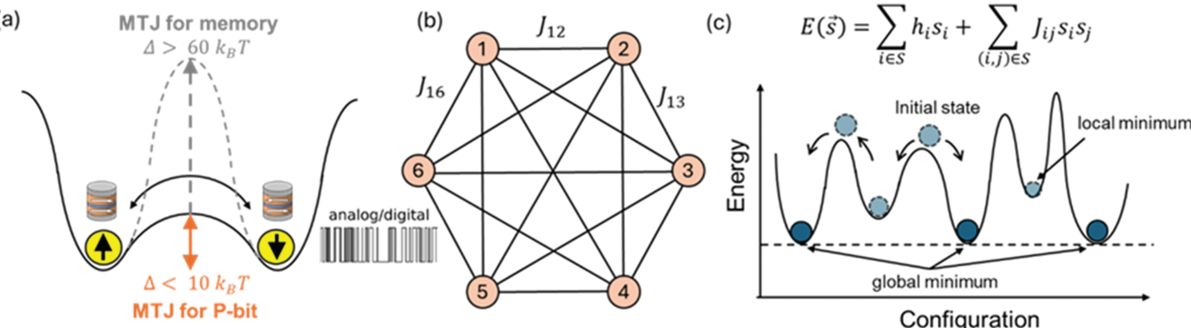


**Figure 11.** Concepts of stochastic MTJ for p-bit and illustration of Ising machine system. (a) Comparison of energy landscape between non-volatile memory application and stochastic-class MTJs. (b) Schematic representation of a fully connected p-bit network implementing an Ising model Hamiltonian. (c) Illustration of thermally activated spin-state transitions in a multi-well energy landscape, demonstrating the system's ability to explore low-energy configurations via stochastic dynamics.

and crossbar architectures to accelerate these operations. At the same time, reconfigurable probabilistic-network fabrics are being developed to dynamically rewire their topology for diverse Hamiltonian problem instances.

Probabilistic computing, by harnessing the intrinsic nanoscale randomness of scalable device platforms such as stochastic MTJs, offers room-temperature, low-power, massively parallel optimization; reversible ('inverse') logic capabilities [289]; seamless integration with proven nanodevices and existing nanofabrication process technologies; and the flexibility to configure many-body interaction networks [290]. Potential applications of p-computing span a wide range of NP-class and combinatorial challenges [291] —protein folding, the traveling-salesman problem, graph 3-colorability, Hamiltonian cycles, Max-Cut, Subset-Sum – as well as machine-learning methods such as Boltzmann-machine sampling, classical and quantum annealing, and Bayesian inference [292] (Figure 12). These capabilities could revolutionize logistics and routing (drones, autonomous vehicles), accelerate drug and vaccine discovery via protein-structure prediction, enhance cybersecurity (encryption/decryption), and drive advanced materials design (molecular dynamics), delivering significant energy and time savings.

Despite its rapid progress, several key challenges remain: ensuring uniform stochastic behavior across large-scale P-bit arrays; co-designing P-bit devices with low-power, high-speed peripheral circuits; adapting probabilistic algorithms to align with specific device characteristics and network constraints; and developing reconfigurable probabilistic fabrics capable of flexibly mapping arbitrary Hamiltonians. Addressing these obstacles requires integrated research efforts across materials science, device physics (spin and other stochastic elements), P-bit I/O circuitry, probabilistic-algorithm design, computational theory, network architecture, circuit engineering, and full-chip integration [293]. Continued advances in these areas will promise to transform applications in optimization, inference, and beyond, ushering in a new era of energy-efficient, high-performance computing.

### 4.3. Skyrmion-based applications

In 1962, British physicist Tony Skyrme introduced a stable, particle-like solution to nonlinear field equations, which later came to be known as a 'skyrmion' [294,295]. More than four decades later, in 2009, S. Mühlbauer et al. [296] experimentally observed a skyrmion lattice for the first time in the bulk chiral magnet MnSi. This lattice was stabilized by the Dzyaloshinskii–Moriya interaction (DMI) arising from the broken inversion symmetry of the cubic B20 crystal structure. Subsequently, in 2011, a skyrmion lattice was identified in a

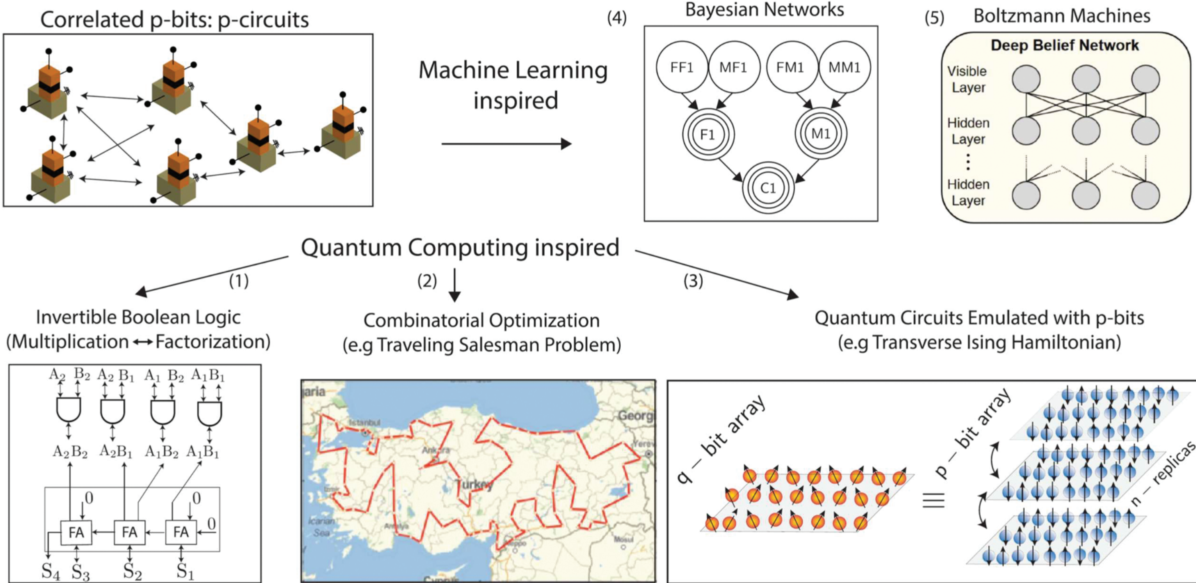


Figure 12. Potential applications of probabilistic computing: Bayesian inference, invertible boolean logic, combinatorial optimization and quantum emulation. The figure is reproduced with permission from ref [291].

monolayer Fe film on an Ir(111) substrate, where interfacial DMI emerges due to symmetry breaking at the interface [297]. Building on these pioneering discoveries, room-temperature individual skyrmions stabilized in thin-film systems were reported between 2015 and 2016 in various perpendicularly magnetized systems, including Co- or Fe-based multilayers and CoFeB/MgO systems [298,299]. These breakthroughs opened new possibilities for incorporating magnetic skyrmions into spintronic applications (Figures 13(a,b)).

A magnetic skyrmion is a topologically protected whirl-like spin texture, characterized by a nontrivial topological invariant known as the skyrmion number $N_{sk}$. In two-dimensional systems, it is defined as [300]:

$$N_{sk} = \frac{1}{4\pi} \int^{\boldsymbol{m}} \cdot \left(\partial_x \boldsymbol{m} \times \partial_y \boldsymbol{m}\right)\, dxdy \tag{6}$$

This topological nature gives rise to many unique physical properties of skyrmions, such as the skyrmion Hall effect, or the topological Hall effect (THE). Moreover, skyrmions offer several advantages for spintronic applications, including ultra-low energy current-driven motion, nanoscale size, high stability, and versatile functionality due to their particle-like behavior. These features make skyrmions promising candidates for next-generation spintronic devices. For instance, A. Fert and colleagues proposed a skyrmion version of racetrack memory, referred to as skyrmion racetrack memory, based on micromagnetic simulations [301]. Their study demonstrated that skyrmion racetrack memory presents significant benefits, such as lower depinning currents, higher storage density due to their nanometer-scale size, and improved robustness against material defects, offering prospects for faster and more energy-efficient spintronic memory technologies.

In order to realize skyrmion-based devices, four essential operations must be implemented: skyrmion generation, deletion, shifting, and detection. All of these operations should be electrically controlled within a

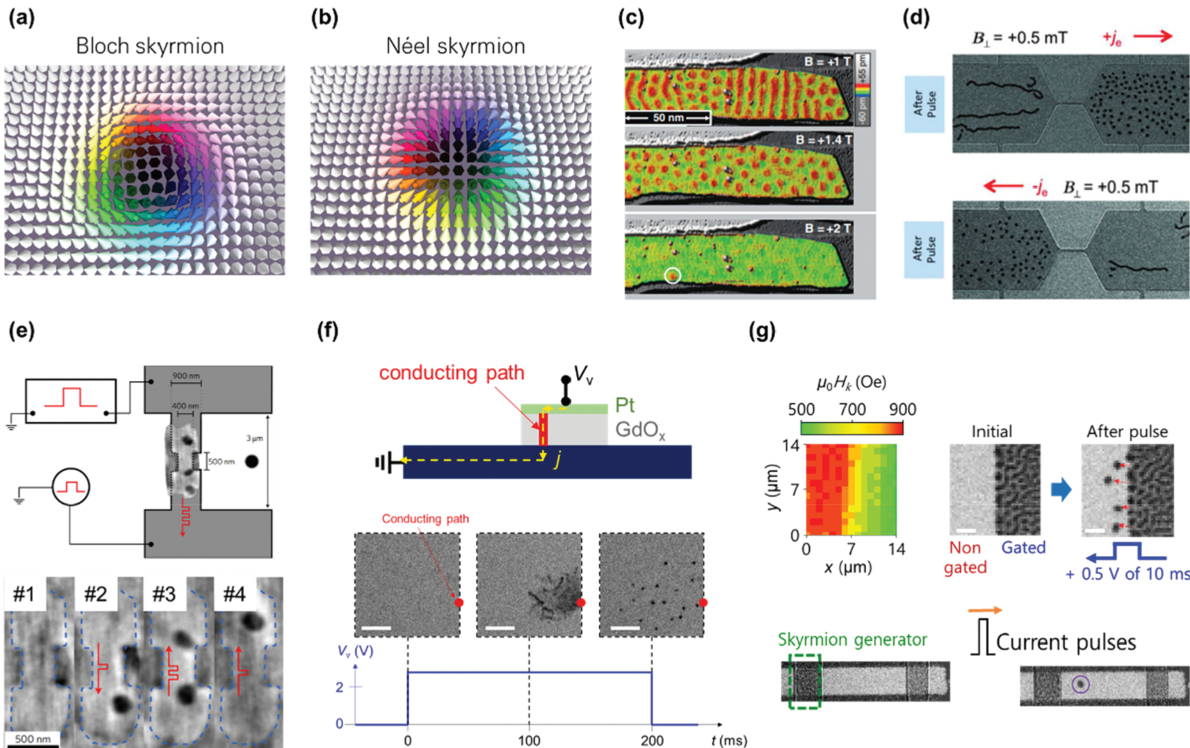


Figure 13. (a, b) schematics of two types of magnetic skyrmions: bloch-type and Néel-type skyrmions. (c) Skyrmions generated electrically by local spin current injection from an STM tip. Reproduced with permission from ref [304]. (d) Skyrmion creation via inhomogeneous current flow in a geometrical constriction. Reproduced with permission from ref [299]. (e) Deterministic skyrmion generation facilitated by defects in a racetrack-like device. Reproduced with permission from ref [305]. (f) Vertical current injection through a breakdown-created path enabling skyrmion formation. Reproduced with permission from ref [307]. (g) Voltage-controlled magnetic anisotropy (VCMA) technique enabling skyrmion generation. Reproduced with permission from ref [308].

single device at room temperature. Here, skyrmion generation refers to the creation of skyrmions at specific, predefined locations rather than randomly or everywhere in the device.

Let's begin with electrical skyrmion generation. One of the earliest ideas for current-induced skyrmion nucleation was to use the Oersted field generated by an electric current. However, this approach is not suitable for practical device applications due to its high-power consumption. Therefore, research has shifted toward spin current-driven magnetization switching mechanisms, such as STT or SOT. Several theoretical proposals for spin current-driven skyrmion generation were introduced in the early stages. For example, J. Iwasaki et al. [302] and J. Sampaio et al. [303] proposed methods for generating skyrmions through spin current injection, supported by micromagnetic simulations and numerical calculations. The first experimental realization of electrically controlled writing and deletion of isolated skyrmions was achieved using a scanning tunneling microscope (STM) at cryogenic temperatures (~4.2 K) [304], where local spin currents enabled manipulation of the spin texture at the atomic scale, as shown in Figure 13(c). Eventually, in 2015, W. Jiang et al. reported room-temperature skyrmion generation driven by SOT, as described in Figure 13(d) [298]. In their work, they employed a patterned device with a geometrical constriction using a Ta/CoFeB/$TaO_x$ trilayer, where current injection led to the transformation of stripe domains into skyrmions by the inhomogeneous current distribution in the constricted region. Further developments in 2017 and 2018 introduced SOT-based deterministic nucleation techniques utilizing defects [305,306]. In these studies, skyrmions were reliably generated within wire-patterned devices, where the same current path could be used for both nucleation and subsequent shifting, as presented in Figure 13(e). This dual functionality represents a key step toward realizing a fully functional skyrmion racetrack memory. A different approach was demonstrated in 2021 by S. Yang et al. [307], who employed a vertical current path formed via electrical breakdown of an insulating layer to nucleate skyrmions, as presented in Figure 13(f). Additionally, a VCMA technique was introduced as another route for skyrmion generation [308]. By locally reducing the PMA, skyrmions were stabilized only within the targeted region, while the surrounding area remained in a uniform magnetic state. A subsequent current pulse then pushed the existing skyrmions into the uniform region, effectively generating isolated skyrmions, as depicted in Figure 13(g).

Next, electrical detection of skyrmions is one of the fundamental operations required for the implementation of skyrmion-based devices. In the early stages of research, detection methods based on the Hall effect were introduced. In 2018, two independent research groups demonstrated electrical detection of skyrmions via the AHE [309,310]. In addition, the THE has also been employed as a means of skyrmion detection, in conjunction with magnetic force microscopy (MFM) [311]. While these approaches represent important milestones in the electrical detection of skyrmions, they are not well suited for integration into practical device architectures. This is primarily due to the inherently small Hall signals, which limit scalability and detection sensitivity. As a result, alternative strategies, such as MTJ structures, are needed to enable efficient and reliable skyrmion readout in realistic device environments. Recently, S. Chen et al. demonstrated electrical readout of skyrmions using MTJs with high signal contrast of 20–70% [312].

Another essential operation is skyrmion shifting. Early demonstrations of SOT-driven skyrmion motion at room temperature were reported in several papers [298,299], where the skyrmion velocity reached up to approximately 50 m/s under a current density of $3.5 \times 10^{11}$ A/m$^2$ [298]. More recently, V. T. Pham et al. showed that the SOT-driven skyrmion velocity can be enhanced up to 900 m/s under a current density of $9.0 \times 10^{11}$ A/m$^2$ by employing a SAF system, as displayed in Figure 14(a) [313]. This approach enables more efficient, high-speed skyrmion transport. In addition, two-dimensional van der Waals (vdW) ferromagnetic systems have also been utilized to demonstrate spin current-driven skyrmion motion. In 2024, Y. Ji et al. reported that skyrmions in a $Fe_3GaTe_2$ system, which is a room temperature vdW ferromagnet, can be driven by STT, as shown in Figure 14(b) [314]. In this system, skyrmion depinning occurred more easily than in conventional thin-film systems, attributed to minimized interface defects from the vdW gaps.

Current-induced skyrmion dynamics is accompanied by the skyrmion Hall effect, which refers to the transverse deflection of skyrmion motion with respect to the driving force direction [300]. This behavior has been experimentally observed in various skyrmion systems [315–317], as described in Figure 14(c). While this phenomenon is intriguing from a fundamental physics perspective, it poses a challenge for device applications, as the transverse motion can lead to unintended skyrmion collisions with device edges, potentially resulting in skyrmion annihilation. To address this issue, considerable efforts have been made to suppress the skyrmion Hall effect. For instance, Y. Hirata et al. demonstrated that the skyrmion Hall effect disappears at

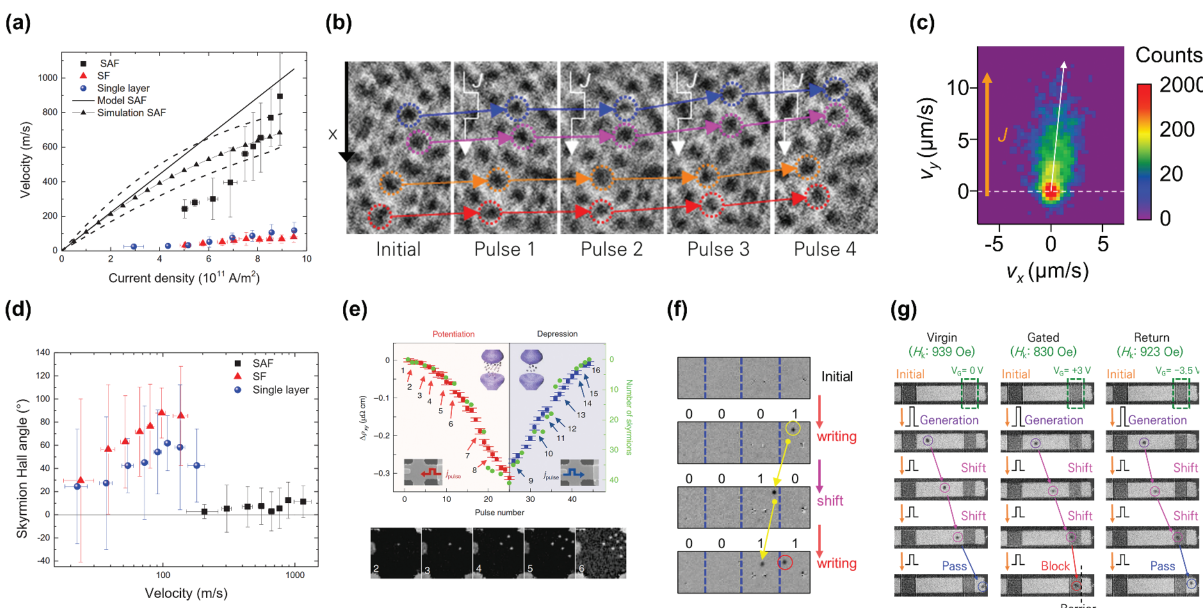


**Figure 14.** (a) High-velocity skyrmion motion realized in SAF structures. Reproduced with permission from ref [313]. (b) STT-induced skyrmion displacement in $Fe_3GaTe_2$ vdW systems. Reproduced with permission from ref [314]. (c) Observation of the skyrmion Hall effect during SOT-driven motion. Reproduced with permission from ref [317]. (d) Skyrmion Hall effect suppression achieved in SAF systems. Reproduced with permission from ref [313]. (e) Key results from skyrmion-based synaptic device demonstrations. Reproduced with permission from ref [320]. (f) Experimental validation of a skyrmion racetrack memory prototype. Reproduced with permission from ref [307]. (g) Demonstration of skyrmion transistor operation. Reproduced with permission from ref [308].

the angular momentum compensation point in ferrimagnetic systems [318]. Additionally, SAF systems have been explored as an effective approach to minimize the skyrmion Hall effect due to the cancellation of the net Magnus forces [313,319], as presented in Figure 14(d).

Based on these foundations, various skyrmion-based spintronic devices have been experimentally demonstrated. For example, K. M. Song et al. introduced a skyrmion-based artificial synapse device, in which the number of skyrmions in a specific region was modulated by injecting current pulses [320] (see Figure 14(e). This, in turn, altered the output signal of an electrical skyrmion detection unit, such as the TMR change in an MTJ, mimicking synaptic plasticity. In addition, a proof-of-concept experiment for skyrmion racetrack memory was presented in 2021 [307], following its initial proposal in 2013 [301], as shown in Figure 14(f). In this work, the authors showed a working demonstration using two separate current paths: one dedicated to skyrmion generation and deletion, and the other for skyrmion shifting. Another example is a skyrmion transistor. In 2015, X. Zhang et al. proposed the concept of a skyrmion transistor where skyrmion motion is controlled by a gate voltage [321]. This concept was experimentally realized in 2023 using a VCMA technique. In their device, skyrmion transport could be passed or blocked, depending on the applied gate voltage, as described in Figure 14(g) [308]. Devices utilizing thermally driven skyrmion dynamics have also been explored. For example, a signal reshuffling device based on thermal diffusive skyrmion dynamics was demonstrated to enable stochastic signal processing [322]. Furthermore, Y. Jibiki et al. implemented a skyrmion Brownian circuit for realizing Brownian computing architectures [323]. Along similar lines, skyrmion-based Brownian reservoir computing has been demonstrated, enabling Boolean logic gate operations and even gesture recognition tasks [324,325]. These demonstrations highlight the enormous potential of skyrmion-based devices across a range of applications. In addition, while many theoretical device concepts have been proposed, a significant number still remain experimentally unrealized. Furthermore, none of the introduced demonstrations above have integrated electrical detection, particularly MTJ-based readout. Therefore, in the near future, fully functional skyrmion devices with integrated detection, as well as new types of skyrmion-based functionalities, are expected to be experimentally realized.

## 5. Conclusion and perspective

MRAM device is built upon two fundamental technologies: magnetoresistance and spin-transfer torque (STT). Significant advancements in magnetoresistance have progressed from anisotropic magnetoresistance (AMR) below 1% in single ferromagnetic layers to tunneling magnetoresistance (TMR) exceeding 600% in MgO-based magnetic tunnel junctions (MTJs). Ongoing research endeavors are critical to achieve high TMR values and strong magnetic anisotropy energy, which are indispensable for enabling MRAM scalability to the nanometer regime. This pursuit actively involves material research for novel ferromagnetic electrodes and tunnel barriers. STT is now considered a mature technology, providing a scalable and efficient writing mechanism for MRAM. As a result, STT-MRAM has transitioned into mass production for non-volatile memory applications. Its inherent advantages, including rapid read/write operations and superior data retention and endurance, underscore its promise for integration into internet-of-things, automotive systems, and data centers. Current industrial development is focused on refining materials and fabrication processes to yield enhanced thermal stability, narrower performance distributions, and reduced failure rates.

New discoveries in spintronics are driving several compelling research directions. Spin-orbit torque (SOT), utilizing spin generation from nonmagnetic materials, presents a novel writing mechanism. SOT-MRAM is particularly promising for cache memory applications, which demand both rapid operation and virtually unlimited endurance. Key challenges for SOT-MRAM development include enhancing SOT efficiency, achieving reliable field-free switching on a large wafer scale, and ensuring compatibility with existing MRAM fabrication techniques. Voltage-controlled magnetic anisotropy (VCMA) is appealing for ultra-low power consumption, but its current limitations – namely, low efficiency in common ferromagnets and the requirement for an external field for deterministic switching – must be addressed. Hybrid approaches combining VCMA with either STT or SOT could offer solutions for reduced power consumption while maintaining high selectivity without external fields. The burgeoning field of orbitronics seeks to electrically manipulate electron's orbital. Current research efforts are primarily dedicated to distinguishing orbital and spin contributions in diverse nonmagnetic systems and establishing their fundamental mechanisms. Future works are demanding to realize the inherent advantages of orbitronics and developing new functionalities unattainable with conventional spintronics. Antiferromagnets provide a vast array of material choices, but their lack of net magnetization has limited their application. Recent studies showed that specific antiferromagnetic spin configurations can enable electrical reading and writing schemes with efficiencies rivaling ferromagnets. To demonstrate their full superiority, further research is needed to confirm attributes like picosecond switching speeds, THz oscillation capabilities, and enhanced stability against field perturbations. Additionally, for scalable wafer-level applications, achieving strong magnetic anisotropy and high ordering temperatures on silicon substrates are critical requirements.

Beyond traditional memory applications, spintronics technology enables novel device applications. Spin-torque oscillators (STOs) represent a key innovation, where sustained precessional dynamics in ferromagnets, driven by STT or SOT, produce radio frequency (RF) signals through magnetoresistance. Their advantages, including nanometer scalability and frequency tunability, position STOs favorably for applications in RF electronics, advanced sensors, and neuromorphic computing. However, challenges such as limited output power, broad linewidths, and device-to-device variability need to be addressed. A particularly exciting frontier is the pursuit of terahertz (THz) oscillators by exploiting the inherently high resonance frequencies of antiferromagnets and ferrimagnets, demanding precise control over spin torque and magnetic damping. Probabilistic computing is another compelling application, offering solutions for complex optimization problems, especially NP-class combinatorial optimizations that are intractable for conventional von Neumann architectures. The magnetic tunnel junction (MTJ), with its energy barrier engineered for stochastic switching, has been utilized as a probabilistic bit platform, leveraging its intrinsic nanoscale randomness and low power characteristics. Critical challenges for probabilistic computing include ensuring uniform stochastic behavior across vast arrays, optimizing individual bits for both low power consumption and high speed, and developing probabilistic algorithms that are well matched to the unique attributes of these devices. In addition, skyrmion-based spintronic devices offer a promising complement to these emerging paradigms, combining topological stability, ultra-low power operation, nanoscale size, and their particle-like nature. These intrinsic features make them well suited for advanced applications such as non-volatile memory, logic-in-memory architectures, and neuromorphic computing. However, realizing their full potential requires overcoming several key challenges,

including deterministic control of motion, suppression of the skyrmion Hall effect, and efficient electrical detection.

## Funding

This work was supported by the National Research Foundation of Korea [2022M3F3A2A03014536]; KIST Institutional Program; National Research Council of Science & Technology [GTL24041-000]; imec Industrial Affiliation Program on MRAM devices.

## Acknowledgments

G.-M. Choi was supported by the National Research Foundation (NRF) of Korea (Grants No. RS-2024-00410027 and No. RS-2025-00519398). O. Lee was supported by the KIST Institutional Program and the National Research Council of Science & Technology (NST) grant by the Korea government (MSIT) (No. GTL24041–000). S.C. acknowledges support from the National Research Foundation of Korea (NRF) grant, funded by the Korean government (MSIT) (Grants 2022M3F3A2A03014536 and RS-2024-00455445). W. Kim was supported by the imec Industrial Affiliation Program on MRAM devices. W. Kim acknowledges the P-line for operational support. B.-G. Park was supported by NRF (No. RS-2022-NR068225). S. Yang was supported by the National Research Council of Science & Technology (NST) grant by the Korea government (MSIT) (No. GTL24041–000).

## Disclosure statement

No potential conflict of interest was reported by the author(s).

## References

[1] Wood R. Future hard disk drive systems. J Magn Magn Mater. 2009;321:555–561. doi: 10.1016/j.jmmm.2008.07.027
[2] Lantz MA, Furrer S, Petermann M, et al. Magnetic tape storage technology. ACM Trans Storage. 2025;21:1–70. doi: 10.1145/3708997
[3] Žutić I, Fabian J, Sarm SD. Spintronics: fundamentals and applications. Rev Mod Phys. 2004;76:323–410. doi: 10.1103/RevModPhys.76.323
[4] Hellman F, Hoffmann A, Tserkovnyak Y, et al. Interface-induced phenomena in magnetism. Rev Mod Phys. 2017;89:025006. doi: 10.1103/RevModPhys.89.025006
[5] Hirohata A, Yamada K, Nakatani Y, et al. Review on spintronics: principles and device applications. J Magn Magn Mater. 2020;509:166711. doi: 10.1016/j.jmmm.2020.166711
[6] Dieny B, Prejbeanu IL, Garell K, et al. Opportunities and challenges for spintronics in the microelectronics industry. Nat Electro. 2020;3:446–459. doi: 10.1038/s41928-020-0461-5
[7] Kawahara T, Ito K, Takemura R, et al. Spin-transfer torque RAM technology: review and prospect. Microelectron Reliab. 2012;52:613–627. doi: 10.1016/j.microrel.2011.09.028
[8] Ikegawa S, Mancoff FB, Aggarwal S. Commercialization of MRAM – historical and future perspective. In: 2021 IEEE International Interconnect Technology Conference (IITC); Kyoto, Japan; 2021. p. 1–3. doi: 10.1109/IITC51362.2021.9537434
[9] McGuire TR, Potter RI. Anisotropic magnetoresistance in ferromagnetic 3d alloys. IEEE Trans Magn. 1975;11:1018–1038. doi: 10.1109/TMAG.1975.1058782
[10] Dahlberg ED, Riggs K, Prinz GA. Magnetotransport: an ideal probe of anisotropy energies in epitaxial films. J Appl Phys. 1999;63:4270–4275. doi: 10.1063/1.340200
[11] Kokado S, Tsunoda M, Harigaya K, et al. Anisotropic magnetoresistance effects in Fe, Co, Ni, Fe4N, and half-metallic ferromagnet: a systematic analysis. J Phys Soc Jpn. 2012;81:024705. doi: 10.1143/JPSJ.81.024705
[12] Ritzinger P, Výborný K. Anisotropic magnetoresistance: materials, models and applications. R Soc Open Sci. 2023;10:230564. doi: 10.1098/rsos.230564
[13] Baibich MN, Broto JM, Fert A, et al. Giant magnetoresistance of (001)Fe/(001)Cr magnetic snperlattices. Phys Rev Lett. 1988;61:2472–2475. doi: 10.1103/PhysRevLett.61.2472
[14] Binasch G, Grünberg F, Zinn W. Enhanced magnetoresistance in layered magnetic structures with antiferromagnetic interlayer exchange. Phys Rev B. 1989;39:4828–4830. doi: 10.1103/PhysRevB.39.4828
[15] Parkin SSP, Li ZG, Smith DJ. Giant magnetoresistance in antiferromagnetic Co/Cu multilayers. Appl Phys Lett. 1991;58:2710–2712. doi: 10.1063/1.104765
[16] Dieny B. Giant magnetoresistance in spin-valve multilayers. J Magn Magn Mater. 1994;136:335–359. doi: 10.1016/0304-8853(94)00356-4
[17] Bass J, Pratt WP. Current-perpendicular (CPP) magnetoresistance in magnetic metallic multilayers. J Magn Magn Mater. 1999;200:274–289.

[18] Julliere M. Tunneling between ferromagnetic films. Phys Lett A. 1975;54:225–226. doi: 10.1016/0375-9601(75)90174-7
[19] Miyazaki T, Tezuka N. Giant magnetic tunneling effect in Fe/Al2O3/Fe junction. J Magn Magn Mater. 1995;139:L231–L234. doi: 10.1016/0304-8853(95)90001-2
[20] Moodera JS, Kinder LR, Wong TM, et al. Large magnetoresistance at room temperature in ferromagnetic thin film tunnel junctions. Phys Rev Lett. 1995;74:3273–3276. doi: 10.1103/PhysRevLett.74.3273
[21] Wang D, Nordman C, Daughton JM, et al. 70% TMR at room temperature for SDT sandwich junctions with CoFeB as free and reference layers. IEEE Trans Magn. 2001;40:2269–2271. doi: 10.1109/TMAG.2004.830219
[22] Acharya J, Goul R, Wu J. High tunneling magnetoresistance in magnetic tunnel junctions with subnanometer thick Al2O3 tunnel barriers fabricated using atomic layer deposition. ACS Appl Mater Interface. 2021;13:15738–15745. doi: 10.1021/acsami.0c03428
[23] Gao L, Jiang X, Rice PM, et al. Enhanced tunneling spin polarization from ultrathin layers of amorphous CoFe. Appl Phys Lett. 2009;95:122503. doi: 10.1063/1.3216050
[24] Karthik SV, Nakatani TM, Rajanikanth A, et al. Spin polarization of Co–Fe alloys estimated by point contact Andreev reflection and tunneling magnetoresistance. J Appl Phys. 2009;105:07C916. doi: 10.1063/1.3058699
[25] Butler WH, Zhang X-G, Schulthess TC, et al. Spin-dependent tunneling conductance of Fe|MgO|Fe sandwiches. Phys Rev B. 2001;63:054416. doi: 10.1103/PhysRevB.63.054416
[26] Mathon J, Umerski A. Theory of tunneling magnetoresistance of an epitaxial Fe/MgO/Fe(001) junction. Phys Rev B. 2001;63:220403(R). doi: 10.1103/PhysRevB.63.220403
[27] Yuasa S, Nagahama T, Fukushima A, et al. Giant room-temperature magnetoresistance in single-crystal Fe/MgO/Fe magnetic tunnel junctions. Nat Mater. 2004;3:868–871. doi: 10.1038/nmat1257
[28] Parkin SSP, Kaiser C, Panchula A, et al. Giant tunnelling magnetoresistance at room temperature with MgO (100) tunnel barriers. Nat Mater. 2004;3:862–867. doi: 10.1038/nmat1256
[29] Yuasa S, Fukushima A, Kubota H, et al. Giant tunneling magnetoresistance up to 410% at room temperature in fully epitaxial Co/MgO/Co magnetic tunnel junctions with bcc Co(001) electrodes. Appl Phys Lett. 2006;89:042505. doi: 10.1063/1.2236268
[30] Scheike T, Xiang Q, Wen Z, et al. Exceeding 400% tunnel magnetoresistance at room temperature in epitaxial Fe/MgO/Fe(001) spin-valve-type magnetic tunnel junctions. Appl Phys Lett. 2021;118:042411. doi: 10.1063/5.0037972
[31] Scheike T, Wen Z, Sukegawa H, et al. 631% room temperature tunnel magnetoresistance with large oscillation effect in CoFe/MgO/CoFe(001) junctions. Appl Phys Lett. 2023;122:112404. doi: 10.1063/5.0145873
[32] Djayaprawira DD, Tsunekawa K, Nagai M, et al. 230% room-temperature magnetoresistance in CoFeB/MgO/CoFeB magnetic tunnel junctions. Appl Phys Lett. 2005;86:092502. doi: 10.1063/1.1871344
[33] Lee YM, Hayakawa J, Ikeda S, et al. Effect of electrode composition on the tunnel magnetoresistance of pseudo-spin-valve magnetic tunnel junction with a MgO tunnel barrier. Appl Phys Lett. 2007;90:212507. doi: 10.1063/1.2742576
[34] Ikeda S, Hayakawa J, Ashizawa Y, et al. Tunnel magnetoresistance of 604% at 300 K by suppression of Ta diffusion in CoFeB/MgO/CoFeB pseudo-spin-valves annealed at high temperature. Appl Phys Lett. 2008;93:082508. doi: 10.1063/1.2976435
[35] Scheike T, Wen Z, Sukegawa H, et al. Enhanced tunnel magnetoresistance in Fe/$Mg_4Al$-$O_x$/Fe(001)magnetic tunnel junctions. Appl Phys Lett. 2022;120:032404. doi: 10.1063/5.0082715
[36] Ikhtiar SH, Xu X. Giant tunnel magnetoresistance in polycrystalline magnetic tunnel junctions with highly textured $MgAl_2O_4$(001) based barriers. Appl Phys Lett. 2018;112:022408. doi: 10.1063/1.5013076
[37] Sukegawa H, Kato Y, Belmoubarik M, et al. $MgGa_2O_4$ spinel barrier for magnetic tunnel junctions: coherent tunneling and low barrier height. Appl Phys Lett. 2017;110:122404. doi: 10.1063/1.4977946
[38] Ikhtiar KS, Cheng P-H, Cheng P-H, et al. Magnetic tunnel junctions with a rock-salt-type $Mg_{1-x}Ti_xO$ barrier for low resistance area product. Appl Phys Lett. 2016;108:242416. doi: 10.1063/1.4953783
[39] Yakushiji K, Kitagawa E, Ochiai T, et al. Fabrication of Mg-X-O (X = Fe, Co, Ni, Cr, Mn, Ti, V, and Zn) barriers for magnetic tunnel junctions. AIP Adv. 2018;8:055905. doi: 10.1063/1.5006099
[40] Scheike T, Sukegawa H, Inomata K, et al. Chemical ordering and large tunnel magnetoresistance in $Co_2FeAl/MgAl_2O_4/Co_2FeAl$(001) junctions. Appl Phys Express. 2016;9:053004. doi: 10.7567/APEX.9.053004
[41] Tezuka N, Ikeda N, Mitsuhashi F, et al. Improved tunnel magnetoresistance of magnetic tunnel junctions with Heusler $Co_2FeAl_{0.5}Si_{0.5}$ electrodes fabricated by molecular beam epitaxy. Appl Phys Lett. 2009;94:162504. doi: 10.1063/1.3116717
[42] Liu H-X, Kawami T, Moges K, et al. Influence of film composition in quaternary Heusler alloy $Co_2$(Mn,Fe)Si thin films on tunnelling magnetoresistance of $Co_2$(Mn,Fe)Si/MgO-based magnetic tunnel junctions. J Phys D. 2015;48:164001. doi: 10.1088/0022-3727/48/16/164001
[43] Ichinose T, Ikeda J, Onoder Y, et al. Large tunnel magnetoresistance in magnetic tunnel junctions with magnetic electrodes of metastable body-centered cubic CoMnFe alloys. J Alloys Compd. 2023;960:170750. doi: 10.1016/j.jallcom.2023.170750

[44] Yoshikawa M, Kitagawa E, Nagase T, et al. Tunnel magnetoresistance over $1_{00}$% in MgO-based magnetic tunnel junction films with perpendicular magnetic $L1_0$-FePt electrodes. IEEE Trans Magn. 2008;44:2573–2576. doi: 10.1109/TMAG.2008.2003059

[45] Suzuki KZ, Mizukami S. Tunnel magnetoresistance exceeding 100% in magnetic tunnel junctions using Mn-based tetragonal alloy electrodes with perpendicular magnetic anisotropy. AIP Adv. 2023;13:035225. doi: 10.1063/5.0141706

[46] Choi G-M, Min B-C, Shin K-H. $L1_0$ ordering of FePtB layers by oxidation-induced stress of capping layer. Appl Phys A. 2013;111:389–394. doi: 10.1007/s00339-012-7512-3

[47] Monso S, Rodmacq B, Auffret S, et al. Crossover from in-plane to perpendicular anisotropy in Pt/CoFe/$AlO_x$ sandwiches as a function of Al oxidation: a very accurate control of the oxidation of tunnel barriers. Appl Phys Lett. 2002;80:4157–4159. doi: 10.1063/1.1483122

[48] Dieny B, Chshiev M. Perpendicular magnetic anisotropy at transition metal/oxide interfaces and applications. Rev Mod Phys. 2017;89:025008. doi: 10.1103/RevModPhys.89.025008

[49] Ikeda S, Miura K, Yamamoto H, et al. A perpendicular-anisotropy CoFeB–MgO magnetic tunnel junction. Nat Mater. 2010;9:721–724. doi: 10.1038/NMAT2804

[50] Johnson M. Spin polarization of gold films via transported (invited). J Appl Phys. 1994;75:6714–6719. doi: 10.1063/1.356848

[51] Jedema FJ, Filip AT, van Wees BJ. Electrical spin injection and accumulation at room temperature in an all-metal mesoscopic spin valve. Nature. 2001;410:345–348. doi: 10.1038/35066533

[52] Rajanikanth A, Kasai S, Ohshima N, et al. Spin polarization of currents in Co/Pt multilayer and Co–Pt alloy thin films. Appl Phys Lett. 2010;97:022505. doi: 10.1063/1.3460910

[53] Slonczewski JC. Current-driven excitation of magnetic multilayers. J Magn Magn Mater. 1996;159:L1–L7. doi: 10.1016/0304-8853(96)00062-5

[54] Berger L. Emission of spin waves by a magnetic multilayer traversed by a current. Phys Rev B. 1996;54:9353–9358. doi: 10.1103/PhysRevB.54.9353

[55] Stiles MD, Zangwill A. Anatomy of spin-transfer torque. Phys Rev B. 2002;66:014407. doi: 10.1103/PhysRevB.66.014407

[56] Slonczewski JC. Currents and torques in metallic magnetic multilayers. J Magn Magn Mater. 2002;247:324–338. doi: 10.1016/S0304-8853(02)00291-3

[57] Ralph DC, Stiles MD. Spin transfer torques. J Magn Magn Mater. 2008;320:1190–1216. doi: 10.1016/j.jmmm.2007.12.019

[58] Kubota H, Kukushima A, Yakushiji K, et al. Quantitative measurement of voltage dependence of spin-transfer torque in MgO-based magnetic tunnel junctions. Nat Phys. 2008;4:37–41. doi: 10.1038/nphys784

[59] Sankey JC, Cui Y-T, Sun JZ, et al. Measurement of the spin-transfer-torque vector in magnetic tunnel junctions. Nat Phys. 2008;4:67–71. doi: 10.1038/nphys783

[60] Oh S-C, Park S-Y, Manchon A, et al. Bias-voltage dependence of perpendicular spin-transfer torque in asymmetric MgO-based magnetic tunnel junctions. Nat Phys. 2009;5:898–902. doi: 10.1038/nphys1427

[61] Sun JZ. Spin-current interaction with a monodomain magnetic body: a model study. Phys Rev B. 2000;62:570–578. doi: 10.1103/PhysRevB.62.570

[62] Devolder T, Hayakawa J, Ito K, et al. Single-shot time-resolved measurements of nanosecond-scale spin-transfer induced switching: stochastic versus deterministic aspects. Phys Rev Lett. 2008;100:057206. doi: 10.1103/PhysRevLett.100.057206

[63] Tomita H, Konishi K, Nozaki T, et al. Single-shot measurements of spin-transfer switching in CoFeB/MgO/CoFeB magnetic tunnel junctions. Appl Phys Express. 2008;1:061303. doi: 10.1143/APEX.1.061303

[64] Katine JA, Alber FJ, Buhrman RA, et al. Current-driven magnetization reversal and spin-wave excitations in Co/Cu/Co pillars. Phys Rev Lett. 2000;84:3149–3152. doi: 10.1103/PhysRevLett.84.3149

[65] Albert FJ, Emley NC, Myers EB, et al. Quantitative study of magnetization reversal by spin-polarized current in magnetic multilayer nanopillars. Phys Rev Lett. 2002;89:226802. doi: 10.1103/PhysRevLett.89.226802

[66] Mangin S, Ravelosona D, Katine JA, et al. Current-induced magnetization reversal in nanopillars with perpendicular anisotropy. Nat Mater. 2006;5:210–215. doi: 10.1038/nmat1595

[67] Tsoi M, Jansen AGM, Bass J, et al. Excitation of a magnetic multilayer by an electric current. Phys Rev Lett. 1998;80:4281–4284. doi: 10.1103/PhysRevLett.80.4281

[68] Kiselev SI, Sankey JC, Krivorotov IN, et al. Microwave oscillations of a nanomagnet driven by a spin-polarized current. Nature. 2003;425:380–383. doi: 10.1038/nature01967

[69] Rippard WH, Pufall MR, Kaka S, et al. Direct-current induced dynamics in $Co_{90}Fe_{10}/Ni_{80}Fe_{20}$ point contacts. Phys Rev Lett. 2004;92:027201. doi: 10.1103/PhysRevLett.92.027201

[70] Krivorotov IN, Emley NC, Sankey JC, et al. Time-domain measurements of nanomagnet dynamics driven by spin-transfer torque. Science. 2005;307:228–231. doi: 10.1126/science.1105722

[71] Hayakawa J, Ikeda S, Lee YM, et al. Current-driven magnetization switching in CoFeB/MgO/CoFeB magnetic tunnel junctions. Jpn J Appl Phys. 2005;44:L1267–L1270. doi: 10.1143/JJAP.44.L1267

[72] Diao Z, Panchula A, Ding Y, et al. Spin transfer switching in dual MgO magnetic tunnel junctions. Appl Phys Lett. 2007;90:132508. doi: 10.1063/1.2717556

[73] Worledge DC. Spin flop switching for magnetic random access memory. Appl Phys Lett. 2004;84:4559–4561. doi: 10.1063/1.1759376
[74] Yoshida C, Takenaga T, Iba Y, et al. Enhanced thermal stability in perpendicular top-pinned magnetic tunnel junction with synthetic antiferromagnetic free layers. IEEE Trans Magn. 2013;49:4363–4366. doi: 10.1109/TMAG.2013.2248350
[75] Diao Z, Li Z, Wang S, et al. Spin-transfer torque switching in magnetic tunnel junctions and spin-transfer torque random access memory. J Phys Condens Matter. 2007;19:165209. doi: 10.1088/0953-8984/19/16/165209
[76] Tulapurkar AA, Suzuki Y, Fukushima A, et al. Spin-torque diode effect in magnetic tunnel junctions. Nature. 2005;438:339–342. doi: 10.1038/nature04207
[77] Nogués J, Schuller IK. Exchange bias. J Magn Magn Mater. 1999;192:203–232. doi: 10.1016/S0304-8853(98)00266-2
[78] Worledge DC, Trouilloud PL. Magnetoresistance measurement of unpatterned magnetic tunnel junction wafers by current-in-plane tunneling. Appl Phys Lett. 2003;83:84–86. doi: 10.1063/1.1590740
[79] Abraham DW, Trouilloud PL, Worledge DC. Rapid-turnaround characterization methods for MRAM development. IBM J Res & Dev. 2006;50:55–67. doi: 10.1147/rd.501.0055
[80] Whitney A, Liu C, Santos TS, et al. Damping in free layers of spin-transfer-torque magnetic memory at elevated temperatures. Phys Rev Appl. 2023;20:034006. doi: 10.1103/PhysRevApplied.20.034006
[81] Richter HJ, Mihajlović G, Chopdekar RV. Thermal effects on damping determination of perpendicular MRAM devices by spin-torque ferromagnetic resonance. J Appl Phys. 2024;136:113902. doi: 10.1063/5.0231388
[82] Peng X, Wakeham S, Morrone A, et al. Towards the sub-50 nm magnetic device definition: ion beam etching (IBE) vs plasma-based etching. Vacuum. 2009;83:1007–1013. doi: 10.1016/j.vacuum.2008.12.003
[83] Islam R, Cui B, Miao G-X. Dry etching strategy of spin-transfer-torque magnetic random access memory: a review. J Vac Sci Technol B. 2020;38:050801. doi: 10.1116/6.0000205
[84] Lim JH, Raghavan N, Kwon JH. Origins and signatures of tail bit failures in ultrathin MgO based STT-MRAM. In: 2020 IEEE International Reliability Physics Symposium (IRPS); Dallas, (TX), USA; 2020. p. 1–5. doi: 10.1109/IRPS45951.2020.9129130
[85] Naik VB, Lee K, Yamane K, et al. Manufacturable 22nm FD-SOI embedded MRAM technology for industrial-grade MCU and IoT applications. In: 2019 IEEE International Electron Devices Meeting (IEDM); San Francisco, (CA), USA; 2019. p..2.3.1–.2.3.4. doi: 10.1109/IEDM19573.2019.8993454
[86] Lee TY, Lee JM, Oh YW, et al. World-most energy-efficient 14nm automotive eMRAM technology for high-endurance applications. In: 2024 IEEE International Electron Devices Meeting (IEDM); San Francisco, (CA), USA; 2024. p. 1–4. doi: 10.1109/IEDM50854.2024.10873518
[87] Ko S, Shim J, Park JH, et al. Key technologies of scaling embedded MRAM to 8nm logic and beyond for automotive application. In: 2024 IEEE International Electron Devices Meeting (IEDM); San Francisco, (CA), USA; 2024. p. 1–4. doi: 10.1109/IEDM50854.2024.10873495
[88] Gallagher WJ, Chien E, Chiang T-W, et al. 22nm STT-MRAM for reflow and automotive uses with high yield, reliability. In: Magnetic Immunity and with Performance and Shielding Options. 2019 IEEE International Electron Devices Meeting (IEDM); San Francisco, (CA), USA; 2019. p.2.7.1–.2.7.4. doi: 10.1109/IEDM19573.2019.8993469
[89] Naik VB, Yamane K, Lee TY, et al. Jedec-qualified highly reliable 22nm FD-SOI embedded MRAM for low-power industrial-grade, and extended performance towards automotive-grade-1 applications. In: 2020 IEEE International Electron Devices Meeting (IEDM); San Francisco, (CA), USA; 2020. p..11.3.1–.11.3.4. doi: 10.1109/IEDM13553.2020.9371935
[90] Lee TY, Yamane K, Otani Y, et al. Advanced MTJ stack engineering of STT-MRAM to realize high speed applications. In: 2020 IEEE International Electron Devices Meeting (IEDM); San Francisco, (CA), USA; 2020. p..11.6.1–.11.6.4. doi: 10.1109/IEDM13553.2020.9372015
[91] Shih Y-C, Lee C-F, Chang Y-A, et al. A reflow-capable, embedded 8Mb STT-MRAM macro with 9ns read access time in 16nm FinFET logic CMOS process. In: 2020 IEEE International Electron Devices Meeting (IEDM); San Francisco, (CA), USA; 2020. p.11.4.1–.11.4.4. doi: 10.1109/IEDM13553.2020.9372115
[92] Jung S, Lee H, Myung S, et al. A crossbar array of magnetoresistive memory devices for in-memory computing. Nature. 2022;601:211–216. doi: 10.1038/s41586-021-04196-6
[93] Dyakonov MI, Perel VI. Current-induced spin orientation of electrons in semiconductors. Phys Lett A. 1971;35:459–460. doi: 10.1016/0375-9601(71)90196-4
[94] Edelstein VM. Spin polarization of conduction electrons induced by electric current in two-dimensional asymmetric electron systems. Solid State Commun. 1990;73:233–235. doi: 10.1016/0038-1098(90)90963-C
[95] Han X, Wang X, Wan C, et al. Spin-orbit torques: materials, physics, and devices. Appl Phys Lett. 2021;118:120502. doi: 10.1063/5.0039147
[96] Kato YK, Myeres RC, Gossard AC, et al. Observation of the spin Hall effect in semiconductors. Science. 2004;306:1910–1913. doi: 10.1126/science.1105514
[97] Wunderlich J, Kaestner B, Sinova J, et al. Experimental observation of the spin-Hall effect in a two-dimensional spin-orbit coupled semiconductor system. Phys Rev Lett. 2005;94:047204. doi: 10.1103/PhysRevLett.94.047204
[98] Ganichev SD, Danilov SN, Schneider P, et al. Electric current-induced spin orientation in quantum well structures. J Magn Magn Mater. 2006;300:127–131. doi: 10.1016/j.jmmm.2005.10.048

[99] Miron IM, Gaudin G, Auffret S, et al. Current-driven spin torque induced by the Rashba effect in a ferromagnetic metal layer. Nat Mater. 2010;9:230–234. doi: 10.1038/NMAT2613

[100] Liu L, Moriyama T, Ralph DC, et al. Spin-torque ferromagnetic resonance induced by the spin Hall effect. Phys Rev Lett. 2011;106:036601. doi: 10.1103/PhysRevLett.106.036601

[101] Miron IM, Garello K, Gaudin G, et al. Perpendicular switching of a single ferromagnetic layer induced by in-plane current injection. Nature. 2011;476:189–193. doi: 10.1038/nature10309

[102] Liu L, Pai C-F, Li Y, et al. Spin-torque switching with the giant spin Hall effect of tantalum. Science. 2012;336:555–558. doi: 10.1126/science.1218197

[103] Lee K-S, Lee S-W, Min B-C, et al. Threshold current for switching of a perpendicular magnetic layer induced by spin Hall effect. Appl Phys Lett. 2013;102:112410. doi: 10.1063/1.4798288

[104] Fang D, Kurebayashi H, Wunderlich J, et al. Spin–orbit-driven ferromagnetic resonance. Nat Nanotech. 2011;6:413–417. doi: 10.1038/NNANO.2011.68

[105] Pi UH, Kim KW, Bae JY, et al. Tilting of the spin orientation induced by Rashba effect in ferromagnetic metal layer. Appl Phys Lett. 2010;97:162507. doi: 10.1063/1.3502596

[106] Avci CO, Garello K, Gabureac M, et al. Interplay of spin-orbit torque and thermoelectric effects in ferromagnet/normal-metal bilayers. Phys Rev B. 2014;90:224427. doi: 10.1103/PhysRevB.90.224427

[107] Fan X, Celik H, Wu J, et al. Quantifying interface and bulk contributions to spin–orbit torque in magnetic bilayers. Nat Commun. 2014;5:3042. doi: 10.1038/ncomms4042

[108] Montazeri M, Upadhyaya P, Onbasli MC, et al. Magneto-optical investigation of spin–orbit torques in metallic and insulating magnetic heterostructures. Nat Commun. 2015;6:8958. doi: 10.1038/ncomms9958

[109] Garello K, Miron IM, Avci CO, et al. Symmetry and magnitude of spin–orbit torques in ferromagnetic heterostructures. Nat Nanotech. 2013;8:587–593. doi: 10.1038/NNANO.2013.145

[110] Kim J, Sinha J, Hayashi M, et al. Layer thickness dependence of the current-induced effective field vector in Ta|CoFeB|MgO. Nat Mater. 2013;12:240–245. doi: 10.1038/nmat3522

[111] Pai C-F, Liu L, Li Y, et al. Spin transfer torque devices utilizing the giant spin Hall effect of tungsten. Appl Phys Lett. 2012;101:122404. doi: 10.1063/1.4753947

[112] Ramaswamy R, Qiu X, Dutta T, et al. Hf thickness dependence of spin-orbit torques in Hf/CoFeB/MgO heterostructures. Appl Phys Lett. 2016;108:202406. doi: 10.1063/1.4951674

[113] Tanaka T, Kontani H, Naito M, et al. Intrinsic spin Hall effect and orbital Hall effect in 4d and 5d transition metals. Phys Rev B. 2008;77:165117. doi: 10.1103/PhysRevB.77.165117

[114] Kontani H, Tanaka T, Hirashima DS, et al. Giant orbital Hall effect in transition metals: origin of large spin and anomalous Hall effects. Phys Rev Lett. 2009;102:016601. doi: 10.1103/PhysRevLett.102.016601

[115] Zhu L, Ralph DC, Buhrman RA. Highly efficient spin-current generation by the spin hall effect in $Au_{1-x}$Ptx. Phys Rev Appl. 2018;10:031001. doi: 10.1103/PhysRevApplied.10.031001

[116] Hu C-Y, Chiu Y-F, Tsai C-C, et al. Toward 100% spin–orbit torque efficiency with high spin–orbital hall conductivity Pt–Cr alloys. ACS Appl Electron Mater. 2022;4:1099–1108. doi: 10.1021/acsaelm.1c01233

[117] Kim GW, Cuong DD, Kim YJ, et al. Spin–orbit torque engineering in β-W/CoFeB heterostructures with W–Ta or W–V alloy layers between β-W and CoFeB. Npg Asia Mater. 2021;13:60. doi: 10.1038/s41427-021-00326-8

[118] Wang P, Migliorini A, Yang S-H, et al. Giant spin Hall effect and spin–orbit torques in 5d transition metal–aluminum alloys from extrinsic scattering. Adv Mater. 2022;34:2109406. doi: 10.1002/adma.202109406

[119] Zhang W, Han W, Yang S-H, et al. Giant facet-dependent spin-orbit torque and spin Hall conductivity in the triangular antiferromagnet IrMn3. Sci Adv. 2016;2:e1600759. doi: 10.1126/sciadv.1600759

[120] Ou Y, Shi S, Ralph DC, et al. Strong spin Hall effect in the antiferromagnet PtMn. Phys Rev B. 2016;93:220405(R). doi: 10.1103/PhysRevB.93.220405

[121] Mellnik AR, Lee JS, Richardell A, et al. Spin-transfer torque generated by a topological insulator. Nature. 2014;511:449–451. doi: 10.1038/nature13534

[122] Wang Y, Zhu D, Wu Y, et al. Room temperature magnetization switching in topological insulator-ferromagnet heterostructures by spin-orbit torques. Nat Commun. 2017;8:1364. doi: 10.1038/s41467-017-01583-4

[123] Dc M, Grassi R, Chen J-Y, et al. Room-temperature high spin–orbit torque due to quantum confinement in sputtered BixSe(1–x) films. Nat Mater. 2018;17:800–807. doi: 10.1038/s41563-018-0136-z

[124] Wu H, Zhang P, Deng P, et al. Room-temperature spin-orbit torque from topological surface states. Phys Rev Lett. 2019;123:207205. doi: 10.1103/PhysRevLett.123.207205

[125] Kim S, Lee H-W, Choi G-M. Giant spin-orbit torque in sputter-deposited Bi films. Adv Sci. 2023;10:2303831. doi: 10.1002/advs.202303831

[126] Yu G, Upadhyay P, Fan Y, et al. Switching of perpendicular magnetization by spin–orbit torques in the absence of external magnetic fields. Nat Nanotech. 2014;9:548–554. doi: 10.1038/NNANO.2014.94

[127] Kang M-G, Choi J-G, Jeong J, et al. Electric-field control of field-free spin-orbit torque switching via laterally modulated Rashba effect in Pt/Co/AlOx structures. Nat Commun. 2021;12:7111. doi: 10.1038/s41467-021-27459-2

[128] You L, Lee O, Bhowmik D, et al. Switching of perpendicularly polarized nanomagnets with spin orbit torque without an external magnetic field by engineering a tilted anisotropy. Proc Natl Acd Sci. 2015;112:10310–10315. doi: 10.1073/pnas.1507474112

[129] Liu L, Zhou C, Shu X, et al. Symmetry-dependent field-free switching of perpendicular magnetization. Nat Nanotechnol. 2021;16:277–282. doi: 10.1038/s41565-020-00826-8
[130] Dc M, Shao D-F, Hou VDH, et al. Observation of anti-damping spin–orbit torques generated by in-plane and out-of-plane spin polarizations in $MnPd_3$. Nat Mater. 2023;22:591–598. doi: 10.1038/s41563-023-01522-3
[131] MacNeill D, Stiehl GM, Guimaraes MHD, et al. Control of spin–orbit torques through crystal symmetry in $WTe_2$/ferromagnet bilayers. Nat Phys. 2017;13:300–305. doi: 10.1038/NPHYS3933
[132] Shi S, Liang S, Zhu Z, et al. All-electric magnetization switching and Dzyaloshinskii–Moriya interaction in $WTe_2$/ferromagnet heterostructures. Nat Nanotechnol. 2019;14:945–949. doi: 10.1038/s41565-019-0525-8
[133] Liang S, Shi S, Hsu C-H, et al. Spin-orbit torque magnetization switching in $MoTe_2$/Permalloy heterostructures. Adv Mater. 2020;32:2002799. doi: 10.1002/adma.202002799
[134] Fukami S, Zhang C, DuttaGupta S, et al. Magnetization switching by spin–orbit torque in an antiferromagnet–ferromagnet bilayer system. Nat Mater. 2016;15:535–541. doi: 10.1038/NMAT4566
[135] Oh Y-W, Back SC, Kim YM, et al. Field-free switching of perpendicular magnetization through spin–orbit torque in antiferromagnet/ferromagnet/oxide structures. Nat Nanotech. 2016;11:878–884. doi: 10.1038/NNANO.2016.109
[136] Wang M, Cai W, Zhu D, et al. Field-free switching of a perpendicular magnetic tunnel junction through the interplay of spin–orbit and spin-transfer torques. Nat Electron. 2018;1:582–588. doi: 10.1038/s41928-018-0160-7
[137] Baek SC, Amin VP, Oh Y-W, et al. Spin currents and spin–orbit torques in ferromagnetic trilayers. Nat Mater. 2018;17:509–513. doi: 10.1038/s41563-018-0041-5
[138] Nguyen VD, Rao S, Wostyn K, et al. Recent progress in spin-orbit torque magnetic random-access memory. Npj Spintronics. 2024;2:48. doi: 10.1038/s44306-024-00044-1
[139] Cukukcu M, Boulle O, Drouard M, et al. Spin-orbit torque magnetization switching of a three-terminal perpendicular magnetic tunnel junction. Appl Phys Lett. 2014;104:042406. doi: 10.1063/1.4863407
[140] Garello K, Yasin F, Couet S, et al. Sot-mram 300mm integration for low power and ultrafast embedded memories. In: 2018 IEEE Symposium on VLSI Circuits; Honolulu, (HI), USA; 2018. p. 81–82. doi: 10.1109/VLSIC.2018.8502269
[141] Maruyama T, Shiota Y, Nozaki T, et al. Large voltage-induced magnetic anisotropy change in a few atomic layers of iron. Nat Nanotech. 2009;4:158–161. doi: 10.1038/NNANO.2008.406
[142] Wang W-G, Li M, Hageman S, et al. Electric-field-assisted switching in magnetic tunnel junctions. Nat Mater. 2012;11:64–68. doi: 10.1038/NMAT3171
[143] Alzate JG, Khalili Amiri P, Upadhyaya P, et al. Voltage-induced switching of nanoscale magnetic tunnel junctions. In: 2012 IEEE International Electron Devices Meeting (IEDM); San Francisco, (CA), USA; 2012. p. 1–4. doi: 10.1109/IEDM.2012.6479130
[144] Kawabe T, Yoshikawa K, Tsujikawa M, et al. Electric-field-induced changes of magnetic moments and magnetocrystalline anisotropy in ultrathin cobalt films. Phys Rev B. 2017;96:220412(R). doi: 10.1103/PhysRevB.96.220412
[145] Wu YC, Kim W, Couet S, et al. Study of precessional switching speed control in voltage-controlled perpendicular magnetic tunnel junction. AIP Adv. 2020;10:035123. doi: 10.1063/5.0002253
[146] One R-A, Béa H, Mican S, et al. Route towards efficient magnetization reversal driven by voltage control of magnetic anisotropy. Sci Rep. 2021;11:8801. doi: 10.1038/s41598-021-88408-z
[147] Shiota Y, Miwa S, Nozaki T, et al. Pulse voltage-induced dynamic magnetization switching in magnetic tunneling junctions with high resistance-area product. Appl Phys Lett. 2012;101:102406. doi: 10.1063/1.4751035
[148] Kanai S, Yamanouchi M, Ikeda S, et al. Electric field-induced magnetization reversal in a perpendicular-anisotropy CoFeB-MgO magnetic tunnel junction. Appl Phys Lett. 2012;101:122403. doi: 10.1063/1.4753816
[149] Wu YC, Kim W, Van Beek S, et al. Impact of ambient temperature on the switching of voltage-controlled perpendicular magnetic tunnel junction. Appl Phys Lett. 2021;118:122404. doi: 10.1063/5.0044995
[150] Shao Y, Lopez-Dominguez V, Davila N, et al. Sub-volt switching of nanoscale voltage-controlled perpendicular magnetic tunnel junctions. Commun Mater. 2022;3:87. doi: 10.1038/s43246-022-00310-x
[151] Favaro D, Kim W, Ranjbar S, et al. Switching of a magnetic tunnel junction by voltage-controlled magnetic anisotropy. Phys Rev Appl. 2025;23:014040. doi: 10.1103/PhysRevApplied.23.014040
[152] Matsumoto R, Nozaki T, Yuasa S, et al. Voltage-induced precessional switching at zero-bias magnetic field in a conically magnetized free layer. Phys Rev Appl. 2018;9:014026. doi: 10.1103/PhysRevApplied.9.014026
[153] Wu YC, Kim W, Garello K, et al. Deterministic and field-free voltage-controlled MRAM for high performance and low power applications. In: 2020 IEEE Symposium on VLSI Technology; Honolulu, (HI), USA; 2020. p. 1–2. doi: 10.1109/VLSITechnology18217.2020.9265057
[154] Carpenter R, Kim W, Sankaran K, et al. Offset field control for VCMA-MRAM. IEEE Trans Nanotechnol. 2023;22:564–568. doi: 10.1109/TNANO.2023.3312949
[155] Ikeura T, Nozaki T, Shiota Y, et al. Reduction in the write error rate of voltage-induced dynamic magnetization switching using the reverse bias method. Jpn J Appl Phys. 2018;57:040311. doi: 10.7567/JJAP.57.040311
[156] Arai H, Hirofuchi T, Imamura H. Probability distribution of the write-error rate of voltage-controlled magnetoresistive random-access memories. Phys Rev Appl. 2021;16:064068. doi: 10.1103/PhysRevApplied.16.064068

[157] Sakai L, Higo Y, Hosomi M, et al. Write error reduction in magnetic tunnel junctions for voltage-controlled magnetoresistive random access memory by using exchange coupled free layer. Appl Phys Lett. 2025;126:022401. doi: 10.1063/5.0241713

[158] Van Beek S, O'Sullivan BJ, Couet S, et al. Understanding and empirical fitting the breakdown of MgO in end-of-line annealed MTJs. In: 2020 IEEE International Reliability Physics Symposium (IRPS); Dallas, (TX), USA; 2020. p. 1–5. doi: 10.1109/IRPS45951.2020.9129551

[159] Nozaki T, Kozioł-Rachwał A, Skowroński W, et al. Large voltage-induced changes in the perpendicular magnetic anisotropy of an MgO-based tunnel junction with an ultrathin Fe layer. Phys Rev Appl. 2016;5:044006. doi: 10.1103/PhysRevApplied.5.044006

[160] Vermeulen BF, Swerts J, Couet S. Electronic voltage control of magnetic anisotropy at room temperature in high-κ SrTiO3/Co/Pt trilayer. Phys Rev Mater. 2020;4:114415. doi: 10.1103/PhysRevMaterials.4.114415

[161] Nozaki T, Yamamoto T, Miwa S, et al. Recent progress in the voltage-controlled magnetic anisotropy effect and the challenges faced in developing voltage-torque MRAM. Micromachines. 2019;10:327. doi: 10.3390/mi10050327

[162] Nozaki T, Endo M, Tsujikawa M, et al. Voltage-controlled magnetic anisotropy in an ultrathin Ir-doped Fe layer with a CoFe termination layer. APL Mater. 2020;8:011108. doi: 10.1063/1.5132626

[163] Carpenter R, Kim W, Sankaran K, et al. Demonstration of a free-layer developed with atomistic simulations enabling BEOL compatible VCMA-MRAM with a coefficient ≥100fJ/Vm. In: 2021 IEEE International Electron Devices Meeting (IEDM); San Francisco, (CA), USA; 2021. p..17.6.1–.17.6.4. doi: 10.1109/IEDM19574.2021.9720579

[164] Li X, Sasaki T, Grezes C, et al. Predictive materials design of magnetic random-access memory based on nanoscale atomic structure and element distribution. Nano Lett. 2019;19:8621–8629. doi: 10.1021/acs.nanolett.9b03190

[165] Nakazawa S, Obinata A, Chiba D, et al. Electric field control of magnetic anisotropy in a Co/Pt bilayer deposited on a high-κ SrTiO3. Appl Phys Lett. 2017;110:062406. doi: 10.1063/1.4976028

[166] Onoda H, Nozaki T, Tamaru S, et al. Enhancing voltage-controlled magnetic anisotropy in Fe80B20/MgO/HfO2 thin films by dielectric constant modulation. Phys Rev Mater. 2022;6. doi: 10.1103/PhysRevMaterials.6.104406

[167] Dorrance R, Alzate JG, Cherepov SS, et al. Diode-MTJ crossbar memory cell using voltage-induced unipolar switching for high-density MRAM. IEEE Electron Device Lett. 2013;34:753–755. doi: 10.1109/LED.2013.2255096

[168] Kanai S, Nakatani Y, Yamanouchi M, et al. Magnetization switching in a CoFeB/MgO magnetic tunnel junction by combining spin-transfer torque and electric field-effect. Appl Phys Lett. 2014;104:212406. doi: 10.1063/1.4880720

[169] Wu YC, Garello K, Kim W, et al. Voltage-gate-assisted spin-orbit-torque magnetic random-access memory for high-density and low-power embedded applications. Phys Rev Appl. 2021;15:064015. doi: 10.1103/PhysRevApplied.15.064015

[170] Tanaka Y, Goto M, Kumar Shukla A, et al. Physically unclonable functions with voltage-controlled magnetic tunnel junctions. IEEE Trans Magn. 2021;57:1–6. doi: 10.1109/TMAG.2020.3042715

[171] Fukushima A, Yamamoto T, Nozaki T, et al. Recent progress in random number generator using voltage pulse-induced switching of nano-magnet: a perspective. APL Mater. 2021;9:030905. doi: 10.1063/5.0038974

[172] Park SR, Kim CH, Yu J, et al. Orbital-angular-momentum based origin of Rashba-type surface band splitting. Phys Rev Lett. 2011;107:156803. doi: 10.1103/PhysRevLett.107.156803

[173] Go D, Hanke J-P, Buhl PM, et al. Toward surface orbitronics: giant orbital magnetism from the orbital Rashba effect at the surface of sp-metals. Sci Rep. 2017;7:46742. doi: 10.1038/srep46742

[174] Salemi L, Berritta M, Nandy AK, et al. Orbitally dominated Rashba–Edelstein effect in noncentrosymmetric antiferromagnets. Nat Commun. 2019;10:5381. doi: 10.1038/s41467-019-13367-z

[175] Hara D, Bahramy MS, Murakami S. Current-induced orbital magnetization in systems without inversion symmetry. Phys Rev B. 2020;102:184404. doi: 10.1103/PhysRevB.102.184404

[176] Go D, Jo D, Kim C, et al. Intrinsic spin and orbital Hall effects from orbital texture. Phys Rev Lett. 2018;121:086602. doi: 10.1103/PhysRevLett.121.086602

[177] Jo D, Go D, Lee H-W. Gigantic intrinsic orbital Hall effects in weakly spin-orbit coupled metals. Phys Rev B. 2018;98:214405. doi: 10.1103/PhysRevB.98.214405

[178] Salemi L, Oppeneer PM. First-principles theory of intrinsic spin and orbital Hall and Nernst effects in metallic monoatomic crystals. Phys Rev Mater. 2022;6:095001. doi: 10.1103/PhysRevMaterials.6.095001

[179] Go D, Lee H-W. Orbital torque: torque generation by orbital current injection. Phys Rev Res. 2020;2:013177. doi: 10.1103/PhysRevResearch.2.013177

[180] An H, Kageyama Y, Kanno Y, et al. Spin–torque generator engineered by natural oxidation of Cu. Nat Commun. 2016;7:13069. doi: 10.1038/ncomms13069

[181] Ding S, Ross A, Go D, et al. Harnessing orbital-to-spin conversion of interfacial orbital currents for efficient spin-orbit torques. Phys Rev Lett. 2020;125:177201. doi: 10.1103/PhysRevLett.125.177201

[182] Kim J, Go D, Tsai H, et al. Nontrivial torque generation by orbital angular momentum injection in ferromagnetic-metal/Cu/Al2O3 trilayers. Phys Rev B. 2021;103:L020407. doi: 10.1103/PhysRevB.103.L020407

[183] Lee D, Go D, Park H-J, et al. Orbital torque in magnetic bilayers. Nat Commun. 2021;12:6710. doi: 10.1038/s41467-021-26650-9

[184] Lee S, Kang M-G, Go D, et al. Efficient conversion of orbital Hall current to spin current for spin-orbit torque switching. Commun Phys. 2021;4:234. doi: 10.1038/s42005-021-00737-7

[185] Sala G, Gambardella P. Giant orbital Hall effect and orbital-to-spin conversion in 3d, 5d, and 4f metallic heterostructures. Phys Rev Res. 2022;4:033037. doi: 10.1103/PhysRevResearch.4.033037
[186] Hayashi H, Jo D, Go D, et al. Observation of long-range orbital transport and giant orbital torque. Commun Phys. 2023;6:32. doi: 10.1038/s42005-023-01139-7
[187] Bose A, Kammerbauer F, Gupta R, Go D, Mokrousov Y, Jakob G and Kläui M. (2023). Detection of long-range orbital-Hall torques. Phys. Rev. B. 107(13). doi:10.1103/PhysRevB.107.134423.
[188] Fukunaga R, Haku S, Hayashi H and Ando K. (2023). Orbital torque originating from orbital Hall effect in Zr. Phys. Rev. Research. 5(2). doi:10.1103/PhysRevResearch.5.023054
[189] Yang Y *et al.* (2024). Orbital torque switching in perpendicularly magnetized materials. Nat Commun. 15(1). doi:10.1038/s41467-024-52824-2
[190] Gupta R, Bouard C, Kammerbauer F, et al. Harnessing orbital hall effect in spin-orbit torque MRAM. Nat Commun. 2025;16:130. doi: 10.1038/s41467-024-55437-x
[191] Hayashi H, Go D, Haku S, et al. Observation of orbital pumping. Nat Electron. 2024;7:646–652. doi: 10.1038/s41928-024-01193-1
[192] Choi Y-G, Jo D, Ko K-H, et al. Observation of the orbital Hall effect in a light metal Ti. Nature. 2023;619:52–56. doi: 10.1038/s41586-023-06101-9
[193] Tserkovnyak Y, Brataas A, Bauer GEW, et al. Nonlocal magnetization dynamics in ferromagnetic heterostructures. Rev Mod Phys. 2005;77:1375–1421. doi: 10.1103/RevModPhys.77.1375
[194] Hamdi AE, Chauleau J-Y, Boselli M, et al. Observation of the orbital inverse Rashba–Edelstein effect. Nat Phys. 2023;19:1855–1860. doi: 10.1038/s41567-023-02121-4
[195] Seifert TS, Go D, Hayashi H, et al. Time-domain observation of ballistic orbital-angular-momentum currents with giant relaxation length in tungsten. Nat Nanotechnol. 2023;18:1132–1138. doi: 10.1038/s41565-023-01470-8
[196] Lyalin I, Alikhah S, Berritta M, et al. Magneto-optical detection of the orbital Hall effect in chromium. Phys Rev Lett. 2023;131:156702. doi: 10.1103/PhysRevLett.131.156702
[197] Marui Y, Kawaguchi M, Sumi S, et al. Spin and orbital Hall currents detected via current-induced magneto-optical Kerr effect in V and Pt. Phys Rev B. 2023;108:144436. doi: 10.1103/PhysRevB.108.144436
[198] Jungwirth T, Marti X, Wadley P, et al. Antiferromagnetic spintronics. Nat Nanotech. 2016;11:231–241. doi: 10.1038/NNANO.2016.18
[199] Baltz V, Manchon A, Tsoi M, et al. Antiferromagnetic spintronics. Rev Mod Phys. 2018;90:015005. doi: 10.1103/RevModPhys.90.015005
[200] Chen H, Liu L, Zhou X, et al. Emerging antiferromagnets for spintronics. Adv Mater. 2024;36:2310379. doi: 10.1002/adma.202310379
[201] Park BG, Wunderlich J, Martí X, et al. A spin-valve-like magnetoresistance of an antiferromagnet-based tunnel junction. Nat Mater. 2011;10:347–351. doi: 10.1038/NMAT2983
[202] Martí X, Park BG, Wunderlich J, et al. Electrical measurement of antiferromagnetic moments in exchange-coupled IrMn/NiFe stacks. Phys Rev Lett. 2012;108:017201. doi: 10.1103/PhysRevLett.108.017201
[203] Fina I, Marti X, Yi D, et al. Anisotropic magnetoresistance in an antiferromagnetic semiconductor. Nat Commun. 2014;5:4671. doi: 10.1038/ncomms5671
[204] Chiang CC, Huang SY, Qu D, et al. Absence of evidence of electrical switching of the antiferromagnetic Néel vector. Phys Rev Lett. 2019;123:227203. doi: 10.1103/PhysRevLett.123.227203
[205] Chen H, Niu Q, MacDonald AH. Anomalous Hall effect arising from noncollinear antiferromagnetism. Phys Rev Lett. 2014;112:017205. doi: 10.1103/PhysRevLett.112.017205
[206] Nakatsuji S, Kiyohara N, Higo T. Large anomalous hall effect in a non-collinear antiferromagnet at room temperature. Nature. 2015;527:212–215. doi: 10.1038/nature15723
[207] Nayak AK, Fischer JE, Sun Y, et al. Large anomalous hall effect driven by a nonvanishing Berry curvature in the noncolinear antiferromagnet Mn3Ge. Sci Adv. 2016;2:e1501870. doi: 10.1126/sciadv.1501870
[208] Kiyohara N, Tomita T, Nakatsuji S. Giant anomalous hall effect in the chiral antiferromagnet Mn3Ge. Phys Rev Appl. 2016;5:064009. doi: 10.1103/PhysRevApplied.5.064009
[209] Zhang Y, Sun Y, Yang H, et al. Strong anisotropic anomalous Hall effect and spin Hall effect in the chiral antiferromagnetic compounds Mn3X (X = Ge, Sn, Ga, Ir, Rh, and Pt). Phys Rev B. 2017;95:075128. doi: 10.1103/PhysRevB.95.075128
[210] Liu ZH, Zhang YJ, Liu GD, et al. Transition from anomalous Hall effect to topological Hall effect in hexagonal non-collinear magnet Mn3Ga. Sci Rep. 2017;7:515. doi: 10.1038/s41598-017-00621-x
[211] Iwaki H, Kimata M, Ikebuchi T, et al. Large anomalous hall effect in L12-ordered antiferromagnetic Mn3Ir thin films. Appl Phys Lett. 2020;116:022408. doi: 10.1063/1.5128241
[212] Zuniga-Cespedes BE, Manna K, Noad HML, et al. Observation of an anomalous hall effect in single-crystal Mn3Pt. New J Phys. 2023;25:023029. doi: 10.1088/1367-2630/acbc3f
[213] Ikhlas M, Tomita T, Koretsune T, et al. Large anomalous nernst effect at room temperature in a chiral antiferromagnet. Nat Phys. 2017;13:1085–1090. doi: 10.1038/NPHYS4181
[214] Higo T, Man H, Gopman DB, et al. Large magneto-optical Kerr effect and imaging of magnetic octupole domains in an antiferromagnetic metal. Nat Photon. 2018;12:73–78. doi: 10.1038/s41566-017-0086-z

[215] Qin P, Yan H, Wang X, et al. Room-temperature magnetoresistance in an all-antiferromagnetic tunnel junction. Nature. 2023;613:485–489. doi: 10.1038/s41586-022-05461-y
[216] Chen X, Higo T, Tanaka K, et al. Octupole-driven magnetoresistance in an antiferromagnetic tunnel junction. Nature. 2023;613:490–495. doi: 10.1038/s41586-022-05463-w
[217] Shi J, Arpaci S, Lopez-Dominguez V, et al. Electrically controlled all-antiferromagnetic tunnel junctions on silicon with large room-temperature magnetoresistance. Adv Mater. 2024;36:2312008. doi: 10.1002/adma.202312008
[218] Železný J, Zhang Y, Felser C, et al. Spin-polarized current in noncollinear antiferromagnets. Phys Rev Lett. 2017;119:187204. doi: 10.1103/PhysRevLett.119.187204
[219] Dong J, Li X, Gurung G, et al. Tunneling magnetoresistance in noncollinear antiferromagnetic tunnel junctions. Phys Rev Lett. 2022;128:197201. doi: 10.1103/PhysRevLett.128.197201
[220] Wadley P, Howells B, Železný J, et al. Electrical switching of an antiferromagnet. Science. 2016;351:587–590. doi: 10.1126/science.aab1031
[221] Bodnar SY, Šmejkal L, Turek I, et al. Writing and reading antiferromagnetic Mn2Au by Néel spin-orbit torques and large anisotropic magnetoresistance. Nat Commun. 2018;9:348. doi: 10.1038/s41467-017-02780-x
[222] Olejník K, Seifert T, Kašpar Z, et al. Terahertz electrical writing speed in an antiferromagnetic memory. Sci Adv. 2018;4:eaar3566. doi: 10.1126/sciadv.aar3566
[223] Tsai H, Higo T, Kondou K, et al. Electrical manipulation of a topological antiferromagnetic state. Nature. 2020;580:608–613. doi: 10.1038/s41586-020-2211-2
[224] Higo T, Kondou K, Nomoto T, et al. Perpendicular full switching of chiral antiferromagnetic order by current. Nature. 2022;607:474–479. doi: 10.1038/s41586-022-04864-1
[225] Takeuchi Y, Yamane Y, Yoon J-Y, et al. Chiral-spin rotation of non-collinear antiferromagnet by spin–orbit torque. Nat Mater. 2021;20:1364–1370. doi: 10.1038/s41563-021-01005-3
[226] Yan GQ, Li S, Lu H, et al. Quantum sensing and imaging of spin–orbit-torque-driven spin dynamics in the non-collinear antiferromagnet Mn3Sn. Adv Mater. 2022;34:220327. doi: 10.1002/adma.202200327
[227] Pal B, Hazra BK, Göbel B, et al. Setting of the magnetic structure of chiral kagome antiferromagnets by a seeded spin-orbit torque. Sci Adv. 2022;8:eabo5930. doi: 10.1126/sciadv.abo5930
[228] Krishnaswamy GK, Sala G, Jacot B, et al. Time-dependent multistate switching of topological antiferromagnetic order in Mn3Sn. Phys Rev Appl. 2022;18:024064. doi: 10.1103/PhysRevApplied.18.024064
[229] Yoon J-Y, Zhang P, Chou C-T, et al. Handedness anomaly in a non-collinear antiferromagnet under spin–orbit torque. Nat Mater. 2023;22:1106–1113. doi: 10.1038/s41563-023-01620-2
[230] Lee W-B, Hwang S, Ko H-W, et al. Spin-torque-driven gigahertz magnetization dynamics in the non-collinear antiferromagnet Mn3Sn. Nat Nanotechnol. 2025;20:487–493. doi: 10.1038/s41565-025-01859-7
[231] Choi HS, Kang SY, Cho SJ, et al. Spin nano–oscillator–based wireless communication. Sci Rep. 2014;4:5486. doi: 10.1038/srep05486
[232] Ruiz-Calaforra A, Purbawati A, Brächer T, etal. Frequency shift keying by current modulation in a MTJ-based STNO with high data rate. Appl. Phys. Lett. 2017;111:082401. doi: 10.1063/1.4994892
[233] Sharma R, Sisodia N, Åkerman J, et al. Enhanced modulation bandwidth of a magnetic tunnel junction-based spin torque nano-oscillator under strong current modulation. IEEE Electron Device Lett. 2021;42:1886–1889. doi: 10.1109/led.2021.3122241
[234] Taniguchi T, Kubota H. Spin torque oscillator for microwave assisted magnetization reversal. Jpn J Appl Phys. 2018;57:053001. doi: 10.7567/jjap.57.053001
[235] Takagishi M, Narita N, Nakagawa Y, et al. Microwave assisted magnetic recording: physics and application to hard disk drives. J Magnetism And Magnetic Mater. 2022;563:169859. doi: 10.1016/j.jmmm.2022.169859
[236] Torrejon J, Riou M, Araujo FA, et al. Neuromorphic computing with nanoscale spintronic oscillators. Nature. 2017;547:428–431. doi: 10.1038/nature23011
[237] Romera M, Talatchian P, Tsunegi S, et al. Vowel recognition with four coupled spin-torque nano-oscillators. Nature. 2018;563:230–234. doi: 10.1038/s41586-018-0632-y
[238] Zahedinejad M, Awad AA, Muralidhar S, et al. Two-dimensional mutually synchronized spin Hall nano-oscillator arrays for neuromorphic computing. Nat Nanotechnol. 2020;15:47–52. doi: 10.1038/s41565-019-0593-9
[239] Demidov VE, Urazhdin S, Demokritov SO. Direct observation and mapping of spin waves emitted by spin-torque nano-oscillators. Nat Mater. 2010;9:984–988. doi: 10.1038/nmat2882
[240] Khymyn R, Lisenkov I, Tiberkevich V, et al. Antiferromagnetic THz-frequency Josephson-like oscillator driven by spin current. Sci Rep. 2017;7:43705. doi: 10.1038/srep43705
[241] Lee DK, Park BG, Lee KJ. Antiferromagnetic oscillators driven by spin currents with arbitrary spin polarization directions. Phys Rev Appl. 2019;11:054048. doi: 10.1103/physrevapplied.11.054048
[242] Lisenkov I, Khymyn R, Åkerman J, et al. Subterahertz ferrimagnetic spin-transfer torque oscillator. Phys Rev B. 2019;100:100409. doi: 10.1103/physrevb.100.100409
[243] Zhong H, Qiao S, Yan S, et al. Terahertz spin-transfer torque oscillator based on a synthetic antiferromagnet. J Magn Magn Mater. 2020;497:166070. doi: 10.1016/j.jmmm.2019.166070
[244] Kaka S, Pufall MR, Rippard WH, et al. Mutual phase-locking of microwave spin torque nano-oscillators. Nature. 2005;437:389–392. doi: 10.1038/nature04035

[245] Mancoff FB, Rizzo ND, Engel BN, et al. Phase-locking in double-point-contact spin-transfer devices. Nature. 2005;437:393–395. doi: 10.1038/nature04036
[246] Madami M, Bonetti S, Consolo G, et al. Direct observation of a propagating spin wave induced by spin-transfer torque. Nat Nanotechnol. 2011;6:635–638. doi: 10.1038/nnano.2011.140
[247] Bonetti S, Tiberkevich V, Consolo G, et al. Experimental evidence of self-localized and propagating spin wave modes in obliquely magnetized current-driven nanocontacts. Phys Rev Lett. 2010;105:217204. doi: 10.1103/physrevlett.105.217204
[248] Mohseni SM, Sani SR, Persson J, et al. Spin torque–generated magnetic droplet solitons. Science. 2013;339:1295–1298. doi: 10.1126/science.1230155
[249] Macià F, Backes D, Kent AD. Stable magnetic droplet solitons in spin-transfer nanocontacts. Nat Nanotechnol. 2014;9:992–996. doi: 10.1038/nnano.2014.255
[250] Chung S, Le QT, Ahlberg M, et al. Direct observation of Zhang-Li torque expansion of magnetic droplet solitons. Phys Rev Lett. 2018;120:217204. doi: 10.1103/physrevlett.120.217204
[251] Deac AM, Fukushima A, Kubota H, et al. Bias-driven high-power microwave emission from MgO-based tunnel magnetoresistance devices. Nat Phys. 2008;4:803–809. doi: 10.1038/nphys1036
[252] Miwa S, Ishibashi S, Tomita H, et al. Highly sensitive nanoscale spin-torque diode. Nat Mater. 2014;13:50–56. doi: 10.1038/NMAT3778
[253] Muduli PK, Heinonen OG, Åkerman J. Bias dependence of perpendicular spin torque and of free- and fixed-layer eigenmodes in MgO-based nanopillars. Phys Rev B. 2011;83:184410. doi: 10.1103/physrevb.83.184410
[254] Demidov VE, Urazhdin S, Edwards ERJ, et al. Control of magnetic fluctuations by spin current. Phys Rev Lett. 2011;107:107204. doi: 10.1103/physrevlett.107.107204
[255] Awad AA, Dürrenfeld P, Houshang A, et al. Long-range mutual synchronization of spin Hall nano-oscillators. Nat Phys. 2017;13:292–299. doi: 10.1038/nphys3927
[256] Zahedinejad M, Fulara H, Khymyn R, et al. Memristive control of mutual spin Hall nano-oscillator synchronization for neuromorphic computing. Nat Mater. 2022;21:81–87. doi: 10.1038/s41563-021-01153-6
[257] Kumar A, Fulara H, Khymyn R, et al. Robust mutual synchronization in long spin Hnano-oscillator chains. Nano Lett. 2023;23:6720–6726. doi: 10.1021/acs.nanolett.3c02036
[258] Kumar A, Chaurasiya AK, González VH, et al. Spin-wave-mediated mutual synchronization and phase tuning in spin Hall nano-oscillators. Nat Phys. 2025;21:245–252. doi: 10.1038/s41567-024-02728-1
[259] Sinha J, Hayashi M, Takahashi YK, et al. Large amplitude microwave emission and reduced nonlinear phase noise in Co2Fe(Ge0.5Ga0.5) Heusler alloy based pseudo spin valve nanopillars. Appl Phys Lett. 2011;99:162508. doi: 10.1063/1.3647771
[260] Seki T, Sakuraba Y, Okura R, et al. High power radio frequency oscillation by spin transfer torque in a Co2MnSi layer: experiment and macrospin simulation. J Appl Phys. 2013;113:033907. doi: 10.1063/1.4776719
[261] Yamamoto T, Seki T, Kubota T, et al. Zero-field spin torque oscillation in Co2(Fe, Mn)Si with a point contact geometry. Appl Phys Lett. 2015;106:092406. doi: 10.1063/1.4914375
[262] Sim CH, Moneck M, Liew T, et al. Frequency-tunable perpendicular spin torque oscillator. J Appl Phys. 2012;111:07C914. doi: 10.1063/1.3677375
[263] Jiang S, Chung S, Le QT, et al. Field-free high-frequency exchange-spring spin-torque nano-oscillators. Nano Lett. 2023;23:1159–1166. doi: 10.1021/acs.nanolett.2c03613
[264] Lebrun R, Tsunegi S, Bortolotti P, et al. Mutual synchronization of spin torque nano-oscillators through a long-range and tunable electrical coupling scheme. Nat Commun. 2017;8:15825. doi: 10.1038/ncomms15825
[265] Erokhin S, Berkov D. Robust synchronization of an arbitrary number of spin-torque-driven vortex nano-oscillators. Phys Rev B. 2014;89:144421. doi: 10.1103/physrevb.89.144421
[266] Flovik V, Macià F, Wahlström E. Describing synchronization and topological excitations in arrays of magnetic spin torque oscillators through the Kuramoto model. Sci Rep. 2016;6:32528. doi: 10.1038/srep32528
[267] Choi JG, Park J, Kang MG, et al. Voltage-driven gigahertz frequency tuning of spin Hall nano-oscillators. Nat Commun. 2022;13:3783. doi: 10.1038/s41467-022-31493-z
[268] Albertsson DI, Zahedinejad M, Houshang A, et al. Ultrafast Ising machines using spin torque nano-oscillators. Appl Phys Lett. 2021;118:112404. doi: 10.1063/5.0041575
[269] McGoldrick BC, Sun JZ, Liu L. Ising machine based on electrically coupled spin Hall nano-oscillators. Phys Rev Appl. 2022;17:014006. doi: 10.1103/physrevapplied.17.014006
[270] Houshang A, Zahedinejad M, Muralidhar S, et al. Phase-binarized spin Hall nano-oscillator arrays: towards spin Hall Ising machines. Phys Rev Appl. 2022;17:014003. doi: 10.1103/physrevapplied.17.014003
[271] Litvinenko A, Khymyn R, González VH, et al. A spinwave Ising machine. Commun Phys. 2023;6:227. doi: 10.1038/s42005-023-01348-0
[272] Mohseni N, McMahon P-L, Byrnes T. Ising machines as hardware solvers of combinatorial optimization problems. Nat Rev Phys. 2022;4:363–379. doi: 10.1038/s42254-022-00440-8
[273] Lucas A. Ising formulations of many NP problems. Front Phys. 2014;2:1–15. doi: 10.3389/fphy.2014.00005
[274] Feynman R-P. Simulating physics with computers. Int J Theor Phys. 1982;21:467–488. doi: 10.1007/BF02650179
[275] Camsari K-Y, Sutton B-M, Datta S. P-bits for probabilistic spin logic. Appl Phys Rev. 2019;6:011305. doi: 10.1063/1.5055860

[276] Cai B, He Y, Xin Y, et al. Unconventional computing based on magnetic tunnel junction. Appl Phys A. 2023;129:236. doi: 10.1007/s00339-022-06365-4
[277] Zink B-R, Lv Y, Wang J-P. Review of magnetic tunnel junctions for stochastic computing. IEEE J Explor Solid-State Comput Devices Circuits. 2022;8:173–184. doi: 10.1109/JXCDC.2022.3227062
[278] Han K-H, Kim Y-J, Koo H-C, et al. Probabilistic computing enabled by continuous random numbers sampled from in-plane magnetized stochastic magnetic tunnel junctions. Appl Phys Lett. 2024;125:142402. doi: 10.1063/5.0223479
[279] Kanai S, Hayakawa K, Ohno H, et al. Theory of relaxation time of stochastic nanomagnets. Phys Rev B. 2021;103:094423. doi: 10.1103/PhysRevB.103.094423
[280] Kim T, Park H-G, Han K-H, et al. Demonstration of in-plane magnetized stochastic magnetic tunnel junction for binary stochastic neuron. AIP Adv. 2022;12:075104. doi: 10.1063/5.0090577
[281] Worledge D-C, Hu G. Spin-transfer torque magnetoresistive random access memory technology status and future directions. Nat Rev Electr Eng. 2024;1:730–747. doi: 10.1038/s44287-024-00111-z
[282] Borders W-A, Pervaiz A-Z, Fukami S, et al. Integer factorization using stochastic magnetic tunnel junctions. Nature. 2019;573:390–393. doi: 10.1038/s41586-019-1557-9
[283] Aadit N-A, Grimaldi A, Carpentieri M, et al. Massively parallel probabilistic computing with sparse Ising machines. Nat Electron. 2022;5:460–468. doi: 10.1038/s41928-022-00774-2
[284] Si J, Yang S, Cen Y, et al. Energy-efficient superparamagnetic Ising machine and its application to traveling salesman problems. Nat Commun. 2024;15:3457. doi: 10.1038/s41467-024-47818-z
[285] Liu Y, Hu Q, Wu Q, et al. Probabilistic circuit implementation based on p-bits using the intrinsic random property of RRAM and p-bit multiplexing strategy. Micromachines. 2022;13:924. doi: 10.3390/mi13060924
[286] Park T-J, Selcuk K, Zhang H-T, et al. Efficient probabilistic computing with stochastic perovskite nickelates. Nano Lett. 2022;22:8654. doi: 10.1021/acs.nanolett.2c03223
[287] Woo K-S, Kim J, Han J, et al. Probabilistic computing using Cu0.1Te0.9/HfO2/Pt diffusive memristors. Nat Commun. 2022;13:5762. doi: 10.1038/s41467-022-33455-x
[288] Singh N-S, Kobayashi K, Cao Q, et al. Cmos plus stochastic nanomagnets enabling heterogeneous computers for probabilistic inference and learning. Nat Commun. 2024;15:2685. doi: 10.1038/s41467-024-46645-6
[289] Camsari K-Y, Faria R, Sutton B-M, et al. Stochastic *p*-bits for invertible logic. Phys Rev X. 2017;7:031014. doi: 10.1103/PhysRevX.7.031014
[290] Finocchio G, Di Ventra M, Camsari K-Y, et al. The promise of spintronics for unconventional computing. J Magnetism And Magnetic Mater. 2021;521:167506. doi: 10.1016/j.jmmm.2020.167506
[291] Camsari K-Y, Debashis P, Ostwal V, et al. From charge to spin and spin to charge: stochastic magnets for probabilistic switching. Proc IEEE. 2020;108:1322–1337. doi: 10.1109/JPROC.2020.2966925
[292] Camsari K-Y, Chowdhury S, Datta S. Scalable emulation of sign-problem–free Hamiltonians with room-temperature *p*-bits. Phys Rev Appl. 2019;12:034061. doi: 10.1103/PhysRevApplied.12.034061
[293] Chowdhury S, Grimaldi A, Aadit N-A, et al. A full-stack view of probabilistic computing with p-bits: devices, architectures, and algorithms. IEEE J Explor Solid-State Comput Devices Circuits. 2023;9:1–11. doi: 10.1109/JXCDC.2023.3256981
[294] Skyrme THR. A non-linear field theory. Proc Roy Soc A. 1961;260:127. doi: 10.1098/rspa.1961.0018
[295] Skyrme THR. A unified field theory of mesons and baryons. Nucl Phys. 1962;31:556. doi: 10.1016/0029-5582(62)90775-7
[296] Muhlbauer S, Binz B, Jonietz F, et al. Skyrmion lattice in a chiral magnet. Science. 2009;323:915. doi: 10.1126/science.1166767
[297] Heinze S, von Bergmann K, Menzel M, et al. Spontaneous atomic-scale magnetic skyrmion lattice in two dimensions. Nat Phys. 2011;7:713. doi: 10.1038/nphys2045
[298] Woo S, Litzius K, Krüger B, et al. Observation of room-temperature magnetic skyrmions and their current-driven dynamics in ultrathin metallic ferromagnets. Nat Mater. 2016;15:501. doi: 10.1038/nmat4593
[299] Jiang W, Upadhyaya P, Zhang W, et al. Blowing magnetic skyrmion bubbles. Science. 2015;349:283. doi: 10.1126/science.aaa1442
[300] Nagaosa N, Tokura Y. Topological properties and dynamics of magnetic skyrmions. Nat Nanotech. 2013;8:899. doi: 10.1038/nnano.2013.243
[301] Fert A, Cros V, Sampaio J, et al. Skyrmions on the track. Nat Nanotech. 2013;8:152. doi: 10.1038/nnano.2013.29
[302] Iwasaki J, Mochizuki M, Nagaosa N, et al. Current-induced skyrmion dynamics in constricted geometries. Nat Nanotech. 2013;8:742. doi: 10.1038/nnano.2013.176
[303] Sampaio J, Cros V, Rohart S, et al. Nucleation, stability and current-induced motion of isolated magnetic skyrmions in nanostructures. Nat Nanotech. 2013;8:839. doi: 10.1038/nnano.2013.210
[304] Romming N, Hanneken C, Menzel M, et al. Writing and deleting single magnetic skyrmions. Science. 2013;341:636. doi: 10.1126/science.1240573
[305] Büttner F, Lemesh I, Schneider M, et al. Field-free deterministic ultrafast creation of magnetic skyrmions by spin–orbit torques. Nat Nanotech. 2017;12:1040. doi: 10.1038/nnano.2017.178
[306] Woo S, Song KM, Zhang X, et al. Deterministic creation and deletion of a single magnetic skyrmion observed by direct time-resolved X-ray microscopy. Nat Electron. 2018;1:288. doi: 10.1038/s41928-018-0070-8

[307] Yang S, Moon KW, Ju T-S, et al. Electrical generation and deletion of magnetic skyrmion-bubbles via vertical current injection. Adv Mater. 2021;33:2104406. doi: 10.1002/adma.202104406
[308] Yang S, Son JW, Ju T-S, et al. Magnetic skyrmion transistor gated with voltage-controlled magnetic anisotropy. Adv Mater. 2023;35:2208881. doi: 10.1002/adma.202208881
[309] Maccariello D, Legrand W, Reyren N. Electrical detection of single magnetic skyrmions in metallic multilayers at room temperature. Nat Nanotech. 2018;13:233. doi: 10.1038/s41565-017-0044-4
[310] Zeissler K, Finizio S, Shahbazi K, et al. Discrete Hall resistivity contribution from Néel skyrmions in multilayer nanodiscs. Nat Nanotech. 2018;13:1161. doi: 10.1038/s41565-018-0268-y
[311] Raju M, Yagil A, Soumyanarayanan A, et al. The evolution of skyrmions in Ir/Fe/Co/Pt multilayers and their topological Hall signature. Nat Commun. 2019;10:696. doi: 10.1038/s41467-018-08041-9
[312] Chen S, Lourembam J, Ho P, et al. All-electrical skyrmionic magnetic tunnel junction. Nature. 2024;627:522. doi: 10.1038/s41586-024-07131-7
[313] Pham VT, Sisodia N, Manici ID, et al. Fast current-induced skyrmion motion in synthetic antiferromagnets. Science. 2024;384:307. doi: 10.1126/science.add5751
[314] Ji Y, Yang S, Ahn H-B, et al. Direct observation of room-temperature magnetic skyrmion motion driven by ultra-low current density in van der Waals ferromagnets. Adv Mater. 2024;36:2312013. doi: 10.1002/adma.202312013
[315] Jiang W, Zhang X, Yu G, et al. Direct observation of the skyrmion Hall effect. Nat Phys. 2017;13:162. doi: 10.1038/nphys3883
[316] Litzius K, Lemesh I, Krüger B, et al. Skyrmion Hall effect revealed by direct time-resolved X-ray microscopy. Nat Phys. 2017;13:170. doi: 10.1038/nphys4000
[317] Yang S, Ju T-S, Kim C, et al. Magnetic field magnitudes needed for skyrmion generation in a general perpendicularly magnetized film. Nano Lett. 2022;22:8430. doi: 10.1021/acs.nanolett.2c02268
[318] Hirata Y, Kim D-H, Kim SK, et al. Vanishing skyrmion Hall effect at the angular momentum compensation temperature of a ferrimagnet. Nat Nanotech. 2019;14:232. doi: 10.1038/s41565-018-0345-2
[319] Dohi T, DuttaGupta S, Fukami S, et al. Formation and current-induced motion of synthetic antiferromagnetic skyrmion bubbles. Nat Commun. 2019;10:5153. doi: 10.1038/s41467-019-13182-6
[320] Song KM, Jeong J-S, Pan B, et al. Skyrmion-based artificial synapses for neuromorphic computing. Nat Electron. 2020;3:148. doi: 10.1038/s41928-020-0385-0
[321] Zhang X, Zhou Y, Ezawa M, et al. Magnetic skyrmion transistor: skyrmion motion in a voltage-gated nanotrack. Sci Rep. 2015;5:11369. doi: 10.1038/srep11369
[322] Zázvorka J, Jakobs F, Heinze D, et al. Thermal skyrmion diffusion used in a reshuffler device. Nat Nanotechnol. 2019;14:658. doi: 10.1038/s41565-019-0436-8
[323] Jibiki Y, Goto M, Tamura E, et al. Skyrmion Brownian circuit implemented in continuous ferromagnetic thin film. Appl Phys Lett. 2020;117:082402. doi: 10.1063/5.0011105
[324] Raab K, Brems MA, Beneke G, et al. Brownian reservoir computing realized using geometrically confined skyrmion dynamics. Nat Commun. 2022;13:6982. doi: 10.1038/s41467-022-34309-2
[325] Beneke G, Winkler TB, Raab K, et al. Gesture recognition with Brownian reservoir computing using geometrically confined skyrmion dynamics. Nat Commun. 2024;15:8103. doi: 10.1038/s41467-024-52345-y